Quantifying the intricacies of biological pattern formation: A new perspective through complexity measures

Jurgen Riedel*, Chris P. Barnes

Department of Cell and Developmental Biology, University College London, London, United Kingdom

Abstract

In this study we examine the emergence of complex biological patterns through the lens of reaction-diffusion systems. We introduce two novel complexity metrics, Diversity of Number of States (DNOS) and Diversity of Pattern Complexity (DPC), which aim to quantify structural intricacies in pattern formation, enhancing traditional linear stability analysis methods. We demonstrate this approach to different systems including the linear Turing, Gray-Scott and FitzHugh-Nagumo models. These measures reveal insights into nonlinear dynamics, multistability, and the conditions under which complex biological patterns stabilize. We then apply the approach to gene regulatory networks, including models of the toggle switch in developmental biology, demonstrating how diffusion and self-activation contribute to robust spatial patterning. Additionally, simulations of the Notch-Delta-EGF signaling pathway in Drosophila neurogenesis highlight the role of gene regulation and parameter variations in modulating pattern complexity and state diversity. Overall, this work establishes complexity-based approaches as valuable tools for exploring the conditions that drive diverse and stable biological pattern formation, offering a pathway for future applications in synthetic biology and tissue engineering.

1 Introduction

A central question in developmental biology is how structure and order arise from initially homogeneous conditions. Reaction–diffusion models have played a major role in addressing this question since Turing's foundational work [Turing, 1952], and the subsequent formulation by Gierer and Meinhardt [Gierer and Meinhardt, 1972]. These models describe the spatial and temporal evolution of interacting chemical species and show how diffusion-driven instabilities can give rise to a wide variety of spatial patterns. Applications span animal coat markings [Staddon, 2024, Kondo et al., 2021], pigment-cell interactions [Nakamasu et al., 2009, Jahanbakhsh and Milinkovitch, 2022], and the influence of geometry and growth on pattern selection [Maini and Woolley, 2019, Alessio and Gupta, 2023]. However, practical challenges

remain, including the integration of detailed biological constraints [Benenson, 2012, Tanaka et al., 2023, Volkening, 2024], the incorporation of growth and deformation [Diez et al., 2023, Werner et al., 2015], and the robustness of pattern formation under uncertain or evolving parameter values [Kondo, 2017, Krause and Gaffney, 2021, Rietkerk et al., 2021, Milinkovitch et al., 2023].

Standard analysis of reaction–diffusion models relies on linear stability theory and bifurcation methods [Maini, 2004]. These techniques determine when a uniform steady state becomes unstable and may give rise to a spatial pattern. They provide important insight but describe only the behaviour near the instability threshold. Recent studies show that instability is not by itself a reliable indicator of persistent pattern formation. Patterns can be transient in systems with multiple stable homogeneous states [Klika, 2017, **?**, Krause, 2024]. In such cases, solutions often return to a homogeneous configuration after a brief period of spatial structure. Extensions that incorporate nonlinear terms can improve predictive power [Chen and Buceta, 2019], but they remain analytically demanding and often system-specific.

Other limitations arise in systems with strong nonlinearities, high-dimensional interactions, or far-from-equilibrium dynamics. Amplitude-equation approaches may fail away from bifurcation points, and deterministic analyses frequently neglect stochastic effects that can influence biological systems [Aragón et al., 2012, Huidobro and Endres, 2024, Pazuki and Endres, 2024]. These challenges motivate complementary ways to characterise patterns that do not require detailed analytical tractability.

Complexity-based methods offer a general framework for describing patterns in terms of their structural detail and state diversity, without relying on predefined geometric categories. Such approaches have been used to compare patterns across models and to quantify nonlinear interactions in biological networks [Paul et al., 2023, van der Kolk et al., 2023, Subbaroyan et al., 2022]. They are applicable to large parameter spaces and can be used to assess the organisation of systems with intricate feedbacks or multistability, including gene regulatory networks [Hagolani et al., 2023, Forestiero, 2022].

Many previous studies of biological patterning have used geometric or morphology-based descriptors tailored to specific systems, such as fish, reptile, or mammalian pigmentation Miyazawa et al. [2010], Lee et al. [2018], Glimm et al. [2021], Moro et al. [2022]. Theoretical work has also examined pattern selection and stability through weakly nonlinear analysis, focusing on transitions between stripes, spots, and labyrinthine motifs and the influence of domain shape Ermentrout [1991], Callahan and Knoblauch [2004]. These methods provide mechanistic insight, but they typically require model-specific derivations and are not easily generalised across distinct systems.

In this work we take a complementary approach. Rather than extracting geometric features or relying on system-specific biological measurements, we analyse the patterns directly through their intensity distributions and information content. This produces a model-independent description that can be applied uniformly across different reaction–diffusion systems and gene regulatory networks. Our aim is to characterise how such systems populate intensity space and how pattern complexity varies across parameter regimes.

Two questions guide this study. First, given a system that becomes unstable and develops spatial structure, what is the character of the pattern that emerges? Second, can we summarise the complexity of these patterns in a way that allows comparison across different

models and parameter sets?

Structure of the paper. Section 4.2 introduces the reaction–diffusion framework and the accompanying linear stability analysis. Section 4.1 summarises the numerical scheme used to integrate the partial differential equations and to generate the pattern ensembles. Section 5 defines the three complexity measures used throughout the study and also describes the auxiliary descriptors based on resistance distances, spectral energy, and wavelet energy, together with the clustering procedures used to identify organisation in the resulting feature spaces. Sections 2.3, 2.4, and 2.5 apply these measures to a linearised reaction–diffusion system and to the Gray–Scott and FitzHugh–Nagumo models, relating regions of parameter space to distinct regimes of state diversity and pattern structure. The subsection *Spatiotemporal patterning enabled by gene regulatory networks* then examines two toggle–switch models with diffusion, with and without self–activation, through Sections 2.6.1 and 2.6.2, using the same complexity measures to organise their patterning behaviour, followed by an analysis of the Notch–Delta–epidermal growth factor signalling model of *Drosophila* neurogenesis. Figure 7 summarises the behaviour of all systems in a common computational space. Section 3 concludes with a discussion of implications, limitations, and possible extensions.

2 Results

2.1 Stability analysis of the Linearised reaction–diffusion system

Turing's original analysis showed how reaction–diffusion systems can break spatial homogeneity through a diffusion-driven instability of a homogeneous steady state Turing [1952]. We use a linear Turing system as an analytically tractable benchmark for stability and length-scale analysis, distinct from the fully nonlinear models used for pattern simulations and complexity measures.

A generic two-species reaction–diffusion system is

$$\frac{\partial u}{\partial t} = D_u \nabla^2 u + f(u, v), \tag{1}$$

$$\frac{\partial v}{\partial t} = D_v \nabla^2 v + g(u, v), \tag{2}$$

where u and v denote the concentrations of an activator and an inhibitor, D_u and D_v are their diffusion coefficients, and f, g encode the local reaction kinetics. Let (h, k) be a homogeneous steady state, so that $f(h, k) = g(h, k) = 0$. Linearising the kinetics around (h, k) yields

$$\frac{\partial u}{\partial t} = a(u - h) + b(v - k) + D_u \nabla^2 u, \tag{3}$$

$$\frac{\partial v}{\partial t} = c(u - h) + d(v - k) + D_v \nabla^2 v, \tag{4}$$

where $a = f_u(h, k)$, $b = f_v(h, k)$, $c = g_u(h, k)$, and $d = g_v(h, k)$ are the entries of the Jacobian of the reaction terms. Thus a and d describe self-feedback of u and v, while b and c are the cross-interaction coefficients.

To analyse linear stability we consider perturbations of the form $(u-h, v-k) \propto \exp(\lambda t + i\mathbf{k}\cdot\mathbf{x})$, which leads to the dispersion relation

$$\lambda_{1,2}(\|\mathbf{k}\|) = \text{eigenvalues of } \begin{pmatrix} a - D_u k^2 & b \\ c & d - D_v k^2 \end{pmatrix}, \qquad k = \|\mathbf{k}\|.$$

For each parameter set (a, b, c, d, D_u, D_v) and wavenumber k we compute the two eigenvalues $\lambda_1(k)$ and $\lambda_2(k)$ numerically. The homogeneous steady state is linearly stable if $\Re\lambda_1(k) < 0$ and $\Re\lambda_2(k) < 0$ for all k; a diffusion-driven (Turing) instability occurs when the homogeneous state is stable at $k = 0$ but $\Re\lambda_i(k) > 0$ for some finite $k > 0$. Saddle-type instabilities correspond to eigenvalues of opposite sign. We classify bifurcations (transcritical, pitchfork, Hopf) by changes in the sign structure and by the emergence of complex-conjugate pairs with vanishing real part as parameters are varied.

The diffusion coefficients D_u and D_v are varied on a logarithmic grid in the range 10^{-5} to 10^{-3}, while the reaction parameters a, b, c, d are sampled uniformly from $[-2, 2]$. For each parameter set we evaluate the dispersion relation on a grid of wavenumbers $k \in [0, 100]$. From the eigenvalues we derive, for each (D_u, D_v), (i) the number of parameter sets that are stable, saddle-like, or undergo a given bifurcation type, and (ii) the dominant pattern length scale, defined as $2\pi/k_{\max}$, where $k_{\max}$ is the wavenumber with maximal growth rate $\max_i \Re\lambda_i(k)$.

Figure 1 summarises these properties over the (D_u, D_v) plane. Colour intensity encodes, for each (D_u, D_v), the density of stable points (A), saddle points (B), pitchfork bifurcations (C), transcritical bifurcations (D), Hopf bifurcations (E), and the dominant pattern length scale (F). This purely linear, spectral analysis delineates regions of parameter space that are expected to support Turing-type pattern formation and provides a reference for the nonlinear models analysed elsewhere in the paper.

The stability analysis provides a spectral description of how perturbations around a homogeneous steady state behave. It identifies regions of parameter space where diffusion-driven instabilities occur, the wavenumbers that grow most strongly, and the types of bifurcations that arise when parameters change. This analysis therefore explains where spatial structure can first emerge and how characteristic length scales are selected.

At the same time, the information obtained from the dispersion relation is necessarily limited to the linear neighbourhood of the steady state. It does not reveal the form of the patterns that develop once nonlinear effects become significant, nor does it quantify how detailed, diverse, or irregular the resulting structures may be. Two parameter sets with similar instability properties can give rise to very different spatial organisations, and instability itself does not ensure that persistent patterns will form. In many cases, the system may transiently create spatial structure before returning to a homogeneous state.

These considerations motivate the use of complementary tools that directly quantify the patterns that are actually produced by the system. The measures introduced in the following section, based on the number of realised intensity states and the compressibility of the spatial field, allow us to summarise the complexity of the final patterns without relying on geometric categories or model-specific features. They provide a view of pattern formation that extends the linear stability picture and enables comparisons across the full parameter range explored in the simulations.

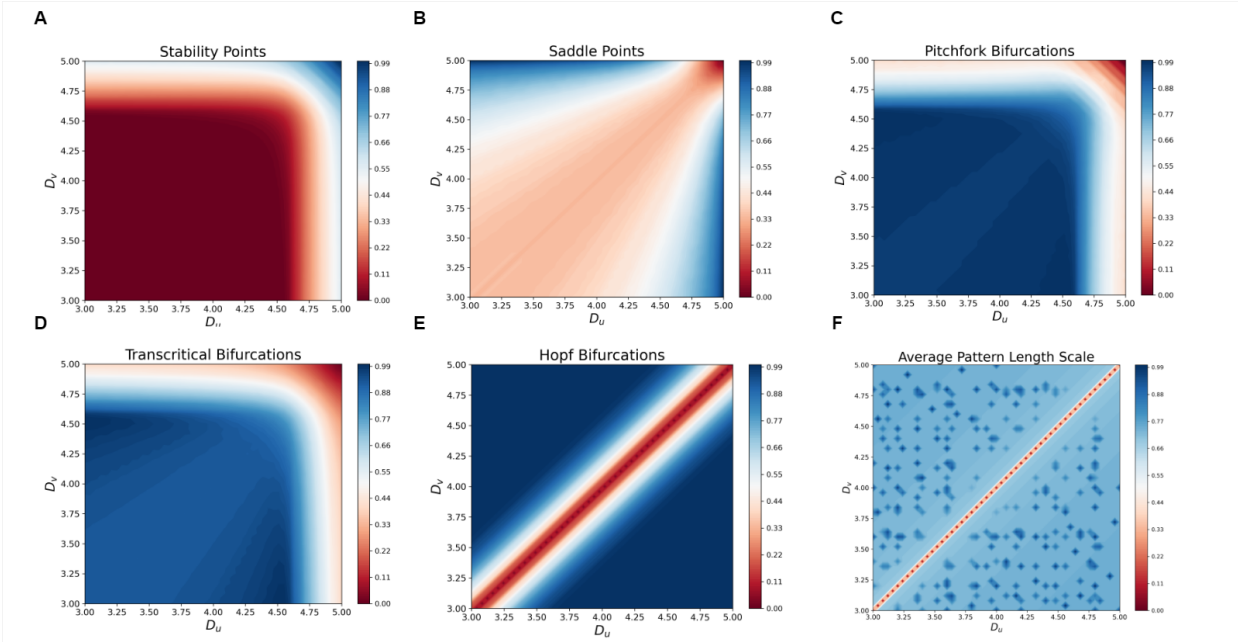

Figure 1: **Stability analysis of the linearised reaction–diffusion system.** The variation in colours across the (D_u, D_v) plane indicates the density of stable points (A), saddle points (B), pitchfork bifurcations (C), transcritical bifurcations (D), Hopf bifurcations (E), and the dominant pattern length scale (F), computed from the dispersion relation of the linearised system. Darker regions correspond to a higher density of parameter sets exhibiting the indicated behaviour.

2.2 Development of new complexity measures

This section introduces our coarse-grained, information–theoretic approach to analysing pattern formation. Rather than focusing on geometric taxonomies (e.g. "spots" versus "stripes"), we quantify how reaction–diffusion systems explore intensity space and generate algorithmically complex patterns. We do so via three complementary measures: the Diversity Number of States (DNOS), the Diversity Pattern Complexity (DPC), and the Uniformity Measure of Entropy (UME). Figure 2 provides an illustrative overview of how the measures DNOS and DPC are constructed; formal definitions and implementation details for all three are given in Section 5 (see in particular Sections 5.1–5.3).

The construction of DNOS begins by normalising the model output to the unit interval, $X(\mathbf{x}) \in [0, 1]$, on a finite pixel grid (typically 80×80 in the schematic example). In the toy illustration of Fig. 2C,D we discretise $[0, 1]$ into a small number of equal-width bins (here $B = 10$), and map each pixel value to its bin index. For example, a state value of 0.013 falls into the $[0.0, 0.1)$ bin, while a value of 0.34 falls into the $[0.3, 0.4)$ bin. The set of distinct bin indices occupied by the pattern then encodes, at a coarse level, how many intensity intervals are actually used. In the Methods (Section 5.1) we keep this *occupied-bin* definition as our operational DNOS, evaluated at a high fixed bin count B^*, and show that it aligns with a more classical entropy-based definition when B is sufficiently large.

The second measure, DPC, quantifies structural complexity via algorithmic compressibility. Starting from the same pixel grid, we convert the field to an image representation and apply a lossless compressor (gzip in the main text), obtaining for each *individual* pattern I

a compression ratio

$$\mathrm{DPC}(I) = \frac{|\mathrm{gzip}(I)|}{|I|},$$

as detailed in Section 5.2. Low DPC values correspond to highly compressible, regular or nearly homogeneous patterns, whereas high DPC values indicate less compressible, algorithmically richer structure. Panels 2A,B use a coarse binning of these per-pattern DPC scores to illustrate how compression ratios are distributed across a collection of patterns, but throughout the paper DPC is treated as a *per-pattern* scalar measure and used directly, without bin-counting, in the regime-identification pipeline.

Finally, we introduce the Uniformity Measure of Entropy (UME) as a complementary descriptor of how evenly a pattern occupies its available intensity (or complexity) space (Section 5.3). Given a binned distribution over B equally spaced intensity bins, with empirical probabilities p_i, UME is defined as the entropy normalised by its maximum possible value,

$$\mathrm{UME}(I) = \frac{-\sum_{i=1}^{B} p_i \log p_i}{\log B},$$

taking the value 1 for perfectly uniform histograms and 0 when all mass is concentrated in a single bin. We apply UME primarily to intensity histograms (providing a notion of how uniformly intensity space is explored, complementing DNOS) and, in auxiliary analyses, to distributions of DPC scores. In this way DNOS captures how many effective states are realised, DPC captures how compressible the resulting spatial configurations are, and UME quantifies how uniformly those states are used. Together, these measures furnish the low-dimensional feature space within which we analyse and compare pattern-forming regimes.

2.3 Exploring the complexity space of the linearised reaction–diffusion system

Having characterised the spectral behaviour of the linearised system, we now examine how the same parameter space is organised when patterns are described through their realised spatial structure. The complexity measures introduced in the preceding section,based on the diversity of occupied intensity states and the compressibility of the final spatial configuration,allow us to evaluate, for each parameter set, the degree of variation and structural richness present in the patterns that emerge after the system evolves beyond the initial linear stage.

This approach addresses a complementary question to the stability analysis. Whereas the dispersion relation identifies parameter combinations that permit the growth of spatial modes, the complexity-based analysis quantifies the patterns that are actually produced once the system has evolved for a finite time in the fully discretised numerical model. The two descriptions therefore capture different aspects of the same system: the linear analysis predicts the onset and preferred wavelength of spatial structure, while the complexity measures summarise the organisation of the resulting patterns across the entire parameter ensemble.

Applied to the linearised Turing model, this dual perspective reveals that the presence of instability is not by itself predictive of the eventual diversity or detail of the patterns. Instead, the complexity measures identify distinct regions in the diffusion plane, with each

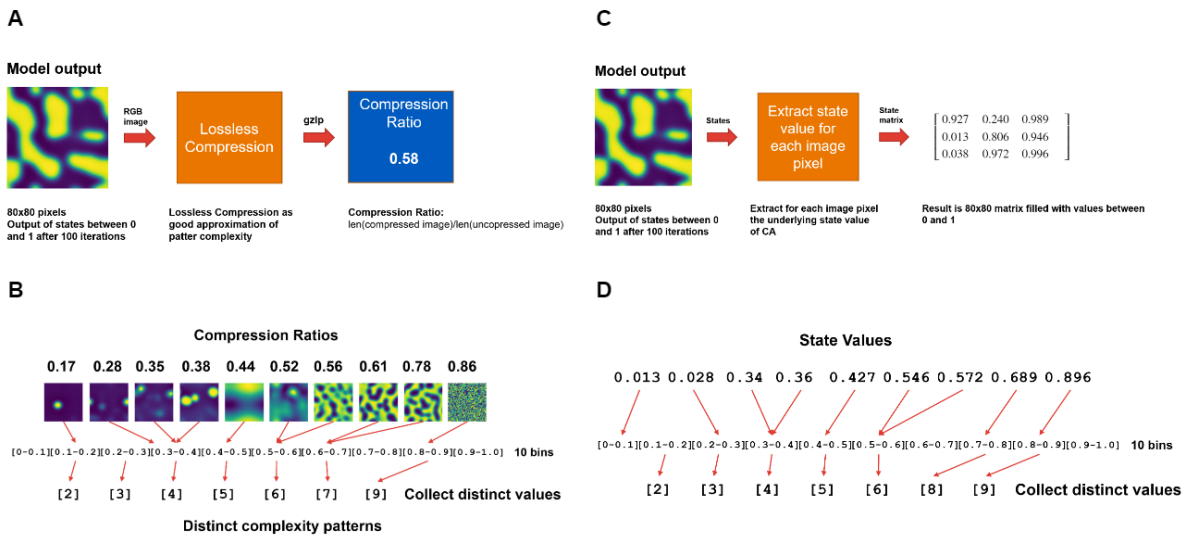

Figure 2: **Schematic construction of the complexity measures. A,B:** Illustration of Discrete Pattern Complexity (DPC). Each pattern is rendered as an image and compressed using a lossless codec (gzip), yielding a per-pattern compression ratio $\mathrm{DPC}(I) = |\mathrm{gzip}(I)|/|I|$. For the schematic we group these ratios into coarse bins to show how complexity scores are distributed across a collection of patterns. **C,D:** Illustration of the Differential Number of States (DNOS). A normalised model output on an 80×80 grid with values in $[0, 1]$ is discretised into a small number of equal-width bins (here $B = 10$ for visual clarity), and each pixel is mapped to its bin index; the set of occupied bins provides an intuitive notion of how many intensity levels are realised. In the Methods (Section 5.1) this occupied-bin definition is evaluated at a much finer resolution B^* and compared with an entropy-based DNOS to verify consistency.

region associated with characteristic levels of state diversity and structural organisation. This organisation is not fully visible from the spectral data alone but becomes clear when DPC and DNOS are examined together.

In this section we numerically solve the PDE system using the finite-difference method (Section 5.6) and revisit the linearised reaction–diffusion system by exploring a comprehensive range of diffusion and reaction parameters to investigate their impact on pattern formation in two-dimensional concentration fields. The parameters and their respective ranges are shown in Table 1.

Parameter	**Description**	**Range**	**Increment**
D_u **(log scale)**	Diffusion rate of u	10^{-3} to 10^{-5}	0.2 (logarithmic)
D_v **(log scale)**	Diffusion rate of v	10^{-3} to 10^{-5}	0.2 (logarithmic)
a	Reaction rate for u	-2 to 2	0.2
b	Interaction of v with u	-2 to 2	0.2
c	Reaction rate for u	-2 to 2	0.2
d	Reaction rate for v	-2 to 2	0.2
dx	Spatial resolution	Computed as 1/SIZE	
dt	Time step	0.02	

Table 1: Summary of the parameters and their ranges explored in the linearised Turing simulations.

In our analysis, we focus on the simulation outputs after 10^3 time steps for all combinations of diffusion coefficients (D_u, D_v) and reaction parameters a, b, c, and d. For each parameter combination, we compute DPC from the gzip compression ratio of the u-field

snapshot (Methods, Section 5.2). To summarise how complexity varies across the (D_u, D_v) grid, we discretise the resulting DPC values to four decimal places (equivalently, into uniform bins at that resolution) and count the number of distinct values observed across all (a, b, c, d) combinations for that (D_u, D_v) pair.

For DNOS, we similarly discretise the u-field concentration values to four decimal places for every reaction-parameter combination, count all distinct values, and average the resulting occupied-bin counts across (a, b, c, d). This procedure is equivalent to evaluating the $\mathrm{DNOS}_{\mathrm{occ}}$ measure defined in the Methods (Section 5.1) at a fixed high intensity resolution. Thus each point in the (D_u, D_v) plane carries a pair of coarse-grained complexity descriptors derived from per-pattern DPC and DNOS values.

We next examine the organisation of these two descriptors by plotting all normalised DPC and DNOS values for all (D_u, D_v) pairs in the feature plane (Figs. 3C–F). All clustering in this study is performed using *k-means*, consistent with the implementation used for every model and figure in the paper. (As discussed in Methods, Section 5.4, Gaussian Mixture Models and hierarchical clustering yield essentially identical partitions.)

To illustrate sensitivity to resolution we show an effective binning into 10^3 bins (Fig. 3C) and 10^4 bins (Fig. 3D). In both cases, four clear clusters emerge. A lower-left cluster (label 1) exhibits low DPC and low DNOS; an upper-left cluster (label 2) has low DPC but high DNOS; and two upper-right clusters (labels 0 and 3) correspond to high DPC and high DNOS. At the coarser resolution the points appear smeared along the DPC axis, whereas the finer resolution produces more compact clusters.

To refine separation,particularly in the high-DPC/high-DNOS corner where cluster 0 appears split,we apply the Uniformity Measure of Entropy (UME; Methods, Section 5.3) before clustering. UME distinguishes patterns with similar bin occupancy but different degrees of uniformity. Including UME yields four sharply separated clusters for both resolutions (Figs. 3E,F), with the high-complexity corner cleanly separating into clusters 0 and 3.

Figures 3A,B show contour plots of the normalised DPC-based and DNOS-based summaries over the (D_u, D_v) plane. Both reveal quadrant-like segmentation, particularly pronounced in the DPC landscape. The lower-left and upper-right quadrants correspond to low complexity, while the upper-left quadrant exhibits the highest complexity.

We then map the k-means cluster assignments back onto the (D_u, D_v) grid (Fig. 3G), showing that the four clusters align cleanly with the diffusion quadrants identified in the contour plots. Clusters 1 and 2 predominantly occur along the diagonal, while clusters 0 and 3 occupy off-diagonal regions.

Finally, to visualise the qualitative patterns underlying each cluster, we extract representative patterns (Fig. 3H). For each (D_u, D_v) assigned to a given cluster, we collect its patterns, scale and discretise them, identify mode patterns in DPC bins, and sample 20 images evenly across the resulting complexity range. Cluster 1 exhibits the lowest diversity (nearly homogeneous states); Cluster 2 shows greater diversity despite low DPC; and Clusters 0 and 3 display rich, multi-scale structures, with Cluster 3 showing the greatest variation across scales.

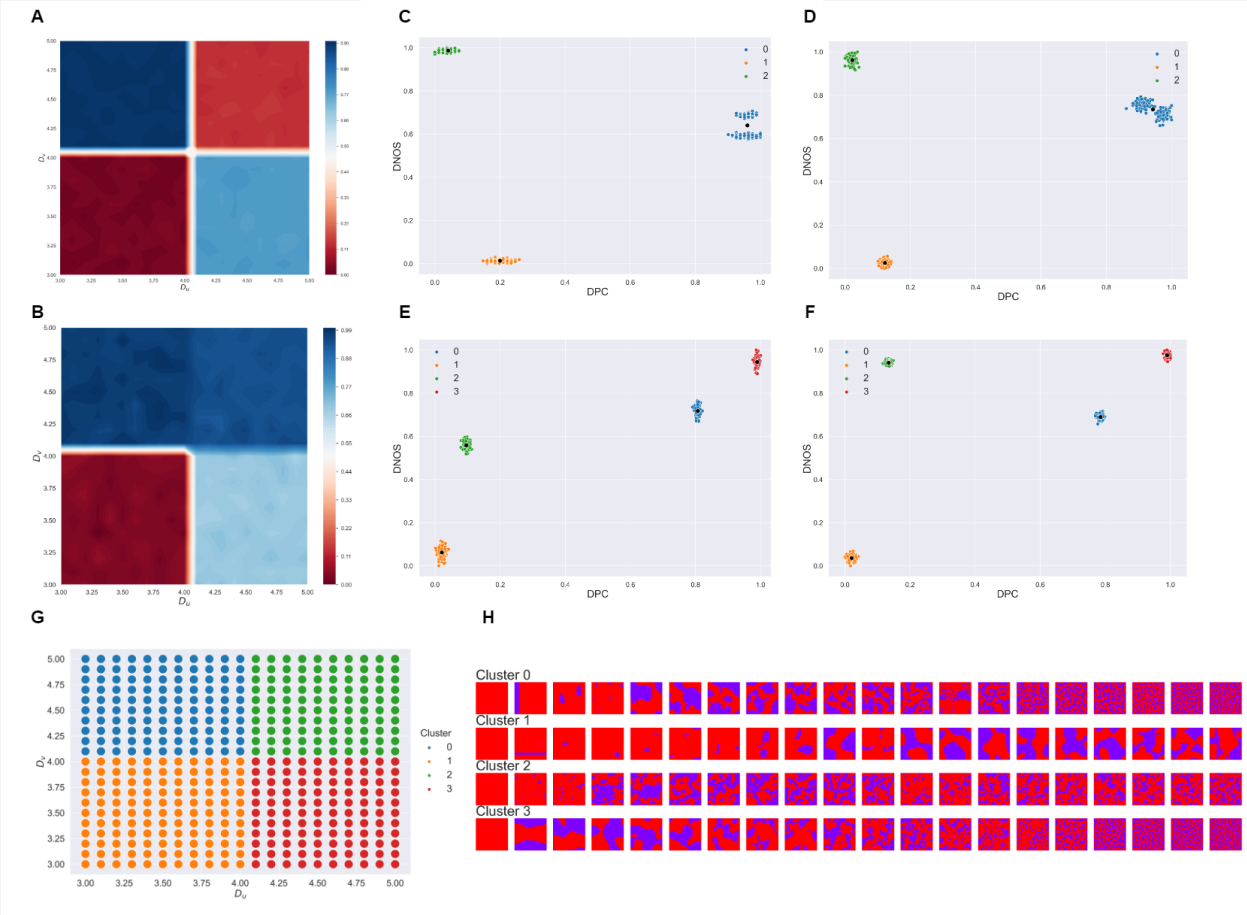

Figure 3: Exploring the complexity space of the linearised reaction–diffusion system. **A,B:** Contour plots of normalised DPC- and DNOS-based summaries over the (D_u, D_v) plane (Methods, Sections 5.2–5.1). **C–F:** Scatter plots of normalised DPC and DNOS for all (D_u, D_v) pairs under two effective resolutions. All clustering shown uses *k-means*; alternative clustering algorithms give equivalent partitions (Methods, Section 5.4). Panels **E,F** incorporate UME (Methods, Section 5.3) as an additional feature, producing sharper separation of regimes. **G:** Mapping cluster assignments from **F** onto the (D_u, D_v) plane. **H:** Representative patterns per cluster, sorted by DPC, illustrating the characteristic variability within each regime. All complexity measures are computed from final-time patterns after transient decay, and the (D_u, D_v) plane is sampled on a refined uniform grid to avoid artefacts from coarse parameter sampling.

2.4 The Gray–Scott model

The Gray–Scott model involves two reacting and diffusing chemical species that produce rich stationary and dynamic spatial patterns. Although the Gray–Scott kinetics were originally introduced as a simplified autocatalytic scheme rather than a literal biochemical pathway Gray and Scott [1983], the model has become a prototypical example of nonlinear reaction–diffusion dynamics exhibiting spots, stripes, labyrinths, and self-replicating structures (e.g. Pearson [1993], Munafo [2018], Mueller and Ben-Jacob [1998]).

Extensive mathematical and computational analyses have clarified the conditions under which these patterns form and persist, highlighting multistability, hysteresis, and complex localised states such as pulses and self-replicating spots McGough and Riley [2004], M. Zheng and Xu [2020], J. Li and Zhang [2019]. As a result, the Gray–Scott model is widely used as a benchmark system for studying pattern formation in chemical, biological, and ecological contexts.

We write the Gray–Scott dynamics in the standard form

$$\frac{\partial u}{\partial t} = D_u \nabla^2 u + f(u,v), \qquad \frac{\partial v}{\partial t} = D_v \nabla^2 v + g(u,v), \tag{5}$$

$$f(u,v) = -uv^2 + \alpha(1-u), \qquad g(u,v) = uv^2 - (\alpha+\beta)v, \tag{6}$$

where u and v are the concentrations of the two species, D_u and D_v are their diffusion coefficients, ∇^2 is the Laplacian, and α, β control feed and removal rates. This representation fits naturally into the general Turing framework introduced earlier.

Parameter	**Description**	**Range**	**Increment**
D_u	Diffusion rate of u	0.1 to 0.2	0.005
D_v	Diffusion rate of v	0.01 to 0.1	0.0045
α	Feed rate	0 to 0.01	0.0005
β	Removal rate	0 to 0.01	0.0005
dx	Spatial resolution	1	
dt	Time step	1	

Table 2: Summary of the parameters and their ranges explored in the Gray–Scott simulations.

Using a similar numerical setup as in Section 2.3, we collect outputs after 10^2 time steps for all combinations of diffusion coefficients (D_u, D_v) and reaction parameters (α, β) (Table 2). For each parameter combination, we compute DPC from the gzip compression ratio of the u-field snapshot and DNOS from the occupied-bin count of the normalised intensity histogram, as defined in the Methods (Sections 5.2 and 5.1).

Figures 4A,F show contour plots of normalised DPC and DNOS values, respectively, over the (D_u, D_v) plane (discretising the underlying arrays at a high effective resolution). To benchmark DPC against established quantitative descriptors of spatial complexity, we also compute three auxiliary measures: Fourier spectral energy (ESP; Methods 5.5.1), wavelet energy ratio (WLE; Methods 5.5.3), and the resistance Distance Histogram (RDH; Methods 5.5.2).

We relate these measures by creating additional contour plots of normalised RDH, ESP, and WLE over the (D_u, D_v) plane (Figs. 4B–D), using the same discretisation procedure as

for DPC and DNOS. Pairwise comparisons of the normalised DPC, RDH, ESP, and WLE arrays are then evaluated using Pearson correlation coefficients (PCC) and mean squared errors (MSE), summarised as heatmaps in Fig. 4E.

The PCC and MSE matrices show a tightly integrated relationship between DPC and other complexity measures such as RDH and WLE, highlighted by exceptionally high correlations (DPC–RDH: 0.965, DPC–WLE: 0.959) and very low MSE values (DPC–RDH: 0.0028, DPC–WLE: 0.0034). This suggests that these measures evaluate closely related dimensions of image complexity, particularly in structural and textural aspects. In contrast, ESP exhibits a lower correlation with DPC (0.265) and correspondingly higher MSE values, indicating that it captures a distinct dimension of complexity that diverges from the properties assessed by DPC, RDH, and WLE. Together, these comparisons show that DPC is at least as pattern-sensitive as classical graph- and wavelet-based descriptors, while also providing additional information beyond purely spectral measures such as ESP.

We next plot all normalised DPC and DNOS values for all (D_u, D_v) pairs in the feature plane (Fig. 4G), using the same (k-means) clustering approach as in the linearised system (Section 2.3). In contrast to the clean quadrant structure observed there (Fig. 3C–F), the Gray–Scott feature space shows more intricate regions, with clusters forming bands and patches spread across the (D_u, D_v) plane. This indicates that some diffusion parameter combinations support markedly higher pattern complexity and diversity than others.

To relate these clusters back to physical parameters, we map the cluster assignments from the DPC–DNOS plane onto the (D_u, D_v) grid (Fig. 4H). As in the linearised reaction–diffusion case (Fig. 3G), the cluster regions partition the parameter space into distinct bands, indicating which diffusion regimes tend to generate more complex and diverse patterns.

Finally, for each cluster around its centroid in DPC–DNOS space, we select 20 representative samples (using the same sampling procedure described in Section 2.3) and display them in a grid, sorted by DPC (Fig. 4I). This visualises the range of spatial phenotypes associated with each computational regime in the Gray–Scott model.

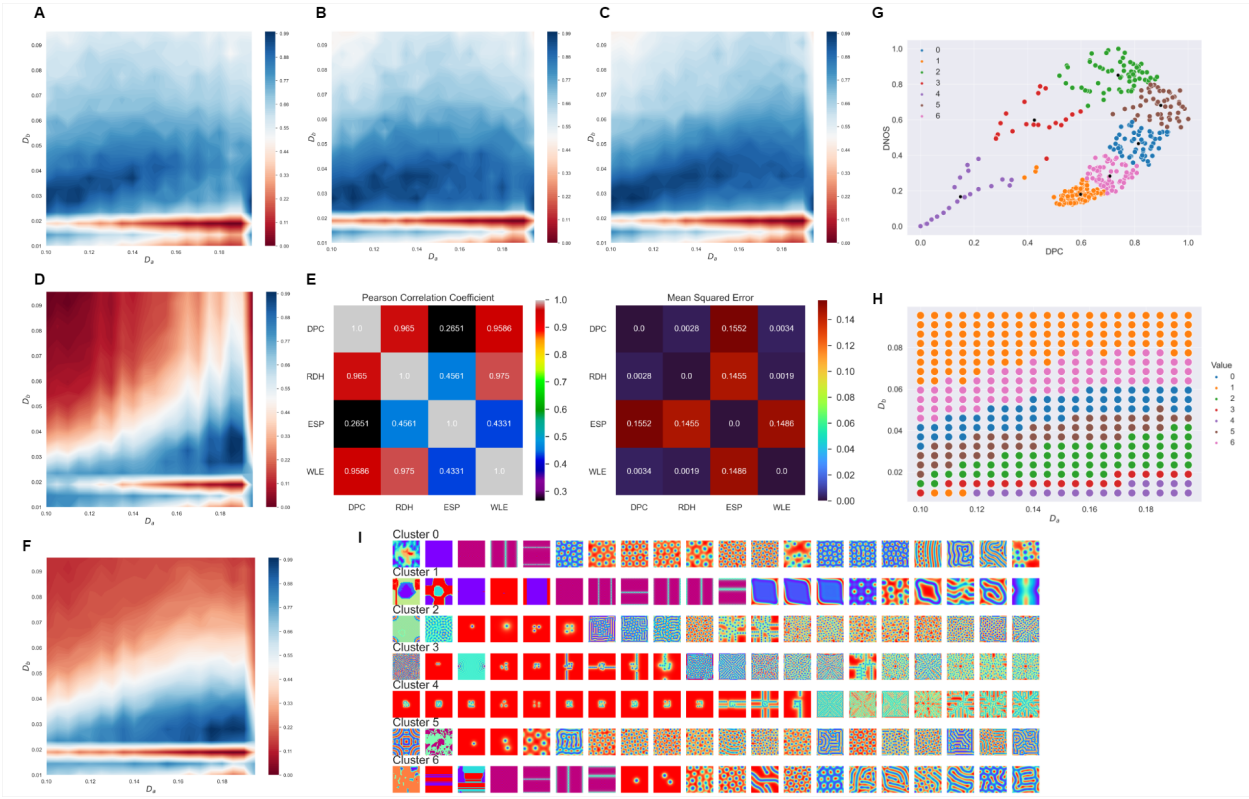

Figure 4: The Gray–Scott model. **A:** Contour plot of normalised DPC values over $D_u \times D_v$. **B–D:** Contour plots of normalised wavelet energy ratio (WLE), resistance distance histogram (RDH), and Fourier spectral energy (ESP), respectively, over the same parameter plane (Methods 5.5.3, 5.5.2, 5.5.1). **E:** Pairwise Pearson correlation coefficients and mean squared errors (MSE) between the normalised DPC, RDH, ESP, and WLE arrays, summarising how DPC relates to these established complexity measures. **F:** Contour plot of normalised DNOS over $D_u \times D_v$. **G:** Scatter plot of normalised DPC versus DNOS for all (D_u, D_v) pairs, with k-means cluster assignments indicated by colour. **H:** Mapping of k-means clusters from **G** back onto the (D_u, D_v) plane. **I:** For each cluster, 20 representative patterns selected around the cluster centroid, sorted by DPC and arranged in a grid, illustrating the diversity of spatial phenotypes within each regime.

2.5 The FitzHugh–Nagumo model

The FitzHugh–Nagumo (FHN) model is a reduced form of the Hodgkin–Huxley equations Hodgkin and Huxley [1952], capturing neuronal excitability through a two–variable system introduced by FitzHugh FitzHugh [1961] and Nagumo Jinichi Nagumo and Yoshizawa [1962]. Its simplicity and canonical cubic nonlinearity make it widely used in neuroscience, cardiology, and reaction–diffusion systems, where it produces travelling waves, oscillations, and Turing patterns (e.g. Daniel Cebrian-Lacasa and Gelens [2024]).

Following Gambino et al. [2018], we use a reaction–diffusion formulation

$$\frac{\partial a}{\partial t} = D_a \nabla^2 a + f(a,b), \qquad f(a,b) = a - a^3 - b + \alpha, \tag{7}$$

$$\frac{\partial b}{\partial t} = D_b \nabla^2 b + g(a,b), \qquad g(a,b) = \beta(a-b), \tag{8}$$

where a acts as an activator and b as an inhibitor. The cubic term $a - a^3$ captures excitable nonlinearity, while $-b$ and $\beta(a-b)$ provide inhibition and coupling. Diffusion coefficients D_a, D_b and parameters α, β control transitions between uniform, oscillatory, and patterned states.

Using the same numerical protocol described for the Gray–Scott model (Section 2.4), we simulated the system across the full parameter grid listed in Table 3, collecting final snapshots after 10^2 time steps.

Parameter	**Description**	**Range**	**Increment**
D_u	Diffusion rate of a	1 to 50	2.5
D_v	Diffusion rate of b	1 to 100	5
α	Activator bias	0 to 0.1	0.005
β	Coupling rate	0 to 0.1	0.005
dx	Spatial resolution	1	
dt	Time step	0.001	

Table 3: Parameter ranges explored in the FitzHugh–Nagumo simulations.

We constructed contour landscapes of normalised DPC and DNOS over the (D_u, D_v) plane (Fig. 5A,F), using the same discretisation procedure as in the previous section. In parallel, we computed the auxiliary descriptors (RDH, ESP, and WLE) defined in Methods (Sections 5.5.2, 5.5.1, 5.5.3) to benchmark DPC against established pattern–complexity measures (Fig. 5B–D).

Pairwise Pearson correlations and mean squared errors (MSE) between the normalised measures are shown in Fig. 5E. DPC exhibits extremely high correlations with RDH ($\rho = 0.994$) and WLE ($\rho = 0.998$), together with very low MSE values (DPC–RDH: 0.00166, DPC–WLE: 0.00029). These near–perfect concordances indicate that DPC captures structural and topological detail almost identically to multiscale (WLE) and graph-based (RDH) descriptors. By contrast, DPC shows weak and slightly negative correlation with ESP ($\rho \approx -0.20$), reflecting that spectral energy emphasises a different dimension of complexity, as already observed for the Gray–Scott model (Section 2.4).

Following the same clustering procedure used in the linear and Gray–Scott analyses, we plot all normalised DPC and DNOS values for all (D_u, D_v) pairs in the feature plane and

assign k-means clusters (Fig. 5G). Distinct bands of increasing DNOS emerge, with cluster 2 (green) occupying the upper right region of the feature space. This suggests that particular diffusion regimes support substantially higher pattern complexity and diversity than others.

Mapping cluster labels back onto parameter space (Fig. 5H) again reveals a structured partitioning of the (D_u, D_v) domain, analogous to the Gray–Scott and linearised systems: clusters form rectangular and banded regions, highlighting parameter regimes that consistently lead to complex patterns.

For each cluster, we select 20 representative patterns around its centroid, using the same sampling protocol as in Section 2.4, and display them sorted by DPC (Fig. 5I). These grids illustrate the characteristic spatial phenotypes associated with each computational regime in the FitzHugh–Nagumo model.

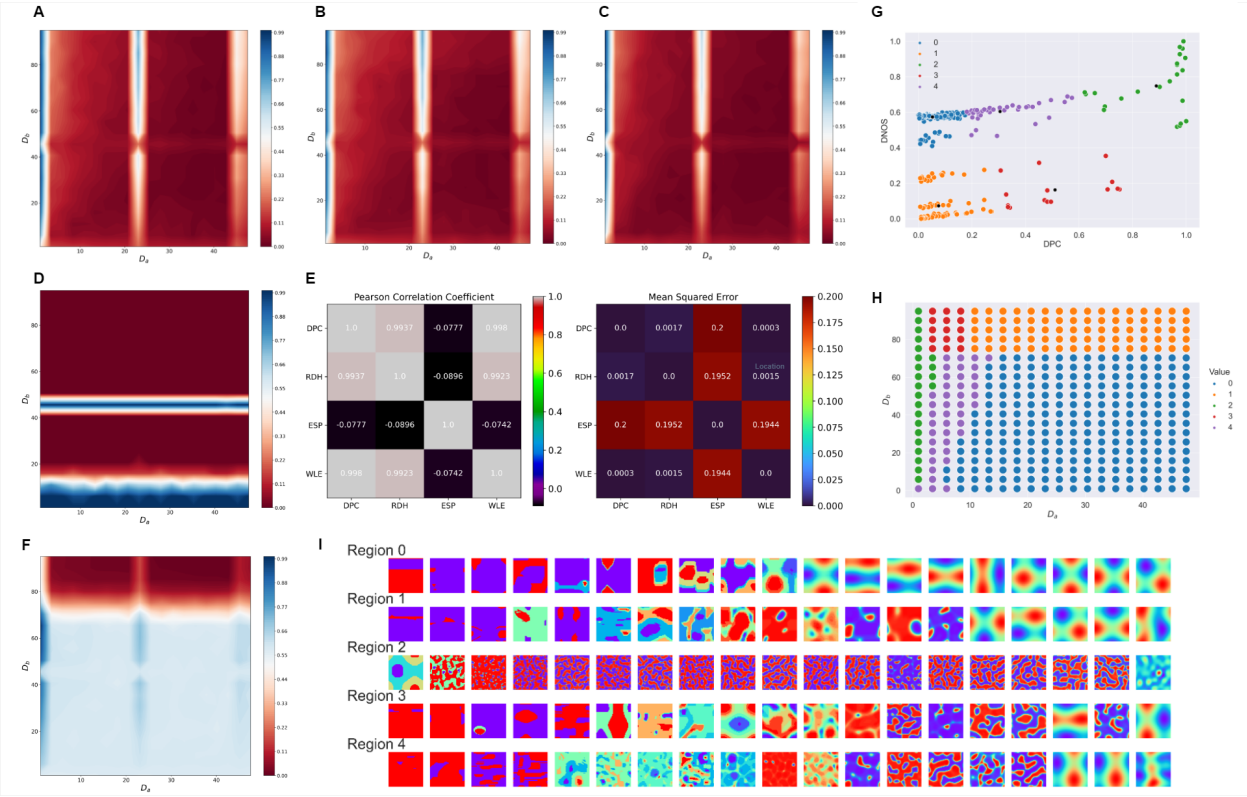

Figure 5: The FitzHugh-Nagumo model: **A-D:** Showing contour plot of normalized DCP, and other pattern complexity measures over $D_u \times D_v$ using discretizing values into 10^4 bins. **A:** DCP **B:** Discretizing wavelet energy ratio (WLE). **C:** Resistance Distance Histogram (RDH). **D:** Discretizing spectral energy (ESP). **E:** Pairwise comparisons of normalized DPC, RDH, ESP, and WLE arrays were evaluated using Pearson correlation coefficients and mean squared errors (MSE). Results are visualized in correlation and MSE heatmaps. **F:** Showing a contour plot of normalized DNOS values over $D_u \times D_v$. **G:** Showing a scatter plot of normalized DPC and DNOS values for all D_u and D_v pairs. Data points were clustered via KMeans. **H:** Mapping the clusters from **G** onto all D_u and D_v., **I:** KMeans clustering was employed to identify representative data points. Images were generated from binned data, 20 representative samples were selected, sorted by complexity, and displayed in a grid organized by cluster.

2.6 Spatiotemporal patterning enabled by gene regulatory networks

Gene regulatory networks (GRNs) are central to spatiotemporal pattern formation in biological systems, governing cell–fate specification, boundary formation, and multicellular organization MacArthur et al. [2009], Paulsson [2004]. Among the canonical GRN motifs is the *toggle switch*, comprising two mutually repressing genes, which generates bistability and enables cells to commit robustly to distinct transcriptional states Roeder and Glauche [2006], Cherry and Adler [2000], ZHO [2011]. A prominent example is the GATA1–PU.1 switch in hematopoiesis, which stabilizes lineage commitment by mutual antagonism of master regulators.

When embedded in a spatially extended medium with 2D diffusion, the toggle switch can generate stable spatial partitions, pinned domain walls, and heterogeneous steady states Perez-Carrasco et al. [2016], Warren and ten Wolde [2004], Kepler and Elston [2001]. Adding positive autoregulation introduces additional attractors (including tristability), increasing both dynamical richness and pattern diversity Chickarmane et al. [2006], Strasser et al. [2011]. Such extensions are relevant for tissue development, lineage branching, and pathological dysregulation such as malignant dedifferentiation Huang et al. [2009].

In the following subsections we analyse two systems introduced in Roy et al. [2023]: (i) a toggle switch with 2D diffusion only, and (ii) a toggle switch with 2D diffusion plus self-activation. Both are explored using the same methodology as in the preceding reaction–diffusion models, with DPC, DNOS, and UME computed as described in Methods (Sections 5.2, 5.1, 5.3). K-means clustering is used, as elsewhere in the paper, to identify computational regimes; Methods includes additional validation using GMM to demonstrate robustness of these partitions.

2.6.1 Toggle switch with 2D diffusion

The toggle-switch dynamics follow

$$\frac{\partial[A]}{\partial t} = D_A \nabla^2[A] + g_A H_{B\to A} - \gamma_A[A], \tag{9}$$

$$\frac{\partial[B]}{\partial t} = D_B \nabla^2[B] + g_B H_{A\to B} - \gamma_B[B], \tag{10}$$

where $H_{X\to Y}$ denotes Hill-type inhibition,

$$H(X; X_0, l, n) = \frac{X_0^n}{X^n + X_0^n} + l\frac{X^n}{X^n + X_0^n},$$

with threshold X_0, fold-change l, and Hill coefficient n. Diffusion coefficients, degradation rates, and production rates are sampled across the ranges listed in the text below, fully matching the experimental setup of Roy et al. [2023].

We simulated the system on a 50×50 grid (5 mm $\times$ 5 mm), with u and v initialised to 100. Diffusion was set to $D = 0.001$, and integration was performed using the finite-difference method (Methods 5.6) for 500 time steps with $dt = 0.1$. Parameters were varied

over: Hill coefficients $n_{A\to B}, n_{B\to A} \in [1, 6]$ (step 0.25), thresholds $A_{0B}, B_{0A} \in [1, 10]$ (step 1), and ten random draws of (γ, g) for each pair of Hill exponents.

Contour plots of normalised DPC and DNOS across this parameter grid are shown in Fig. 6A,B. DPC exhibits diagonal bands of high and low complexity, indicating alternating parameter regimes in which diffusion and bistability promote or suppress spatial patterning. By contrast, DNOS remains uniformly low across nearly the entire space, suggesting that although patterns differ in compressibility (DPC), they occupy only a narrow subset of intensity space and thus exhibit limited state diversity.

The DPC–DNOS scatter plot (Fig. 6C), with K-means clustering, shows that most solutions fall into a low-DNOS regime (DNOS < 0.2) but span a broad range of DPC values. Clusters 0,1,2,6 correspond to this broad low-diversity regime with distinct levels of structural complexity. Cluster 5 shows moderate DNOS with modest complexity, while clusters 3 and 4 exhibit substantially higher DNOS, indicating richer state diversity. Cluster 4, which achieves both high DNOS and high DPC, corresponds to the most complex spatial configurations produced by this model. Overall, the toggle switch with diffusion generates a wide array of pattern complexities despite operating within a strongly constrained state space.

2.6.2 Toggle switch with 2D diffusion and self-activation

Adding positive autoregulation modifies the PDEs to

$$\frac{\partial[A]}{\partial t} = D_A \nabla^2[A] + g_A\, H_{A\to A}\, H_{B\to A} - \gamma_A[A], \tag{11}$$

$$\frac{\partial[B]}{\partial t} = D_B \nabla^2[B] + g_B\, H_{B\to B}\, H_{A\to B} - \gamma_B[B], \tag{12}$$

with $H_{A\to A}$ and $H_{B\to B}$ representing self-activation (Hill-type positive feedback), and with the same Hill-function form as above.

Simulations were performed on a 20×20 grid (2 mm $\times$ 2 mm) for 5000 time steps, with diffusion coefficient $D = 10^{-5}$. Parameters were sampled across: $n_{A\to A}, n_{A\to B} \in [1, 6]$ (step 0.2), thresholds $A_{0A}, A_{0B} \in [1, 6]$ (step 0.25), fold changes $\lambda_{A\to A} = 3.0$, $\lambda_{A\to B} = 0.1$, and random draws of (γ, g) following Roy et al. [2023].

Contour plots of normalised DPC and DNOS (Fig. 6E,F) reveal markedly richer structure than in the non-self-activating case. DPC again forms diagonal bands, but the transitions between high- and low-complexity regions are much more sharply defined. Unlike the 2D-diffusion-only model, DNOS now also separates into distinct regions of high and low diversity, indicating that self-activation enables the system to explore a significantly larger effective state space.

The DPC–DNOS scatter plot (Fig. 6G) shows a clear positive correlation between pattern complexity and state diversity. Six k-means clusters are identified, ranging from low-complexity/low-DNOS (simple patterns, few states) to high-complexity/high-DNOS (rich, multistate patterns). Intermediate clusters (e.g. cluster 0) exhibit moderate DPC and DNOS, corresponding to parameter regimes where spatial organisation is non-trivial even though bistability is only partially resolved by diffusion.

Overall, the self-activating toggle switch supports substantially richer dynamical regimes than its bistable counterpart. Whereas the basic toggle switch exhibits complexity largely

independent of state diversity, the self-activating system jointly elevates both DPC and DNOS, yielding a broad repertoire of spatial patterns and distinct parameter regions in the (D_u, D_v) and DPC–DNOS planes.

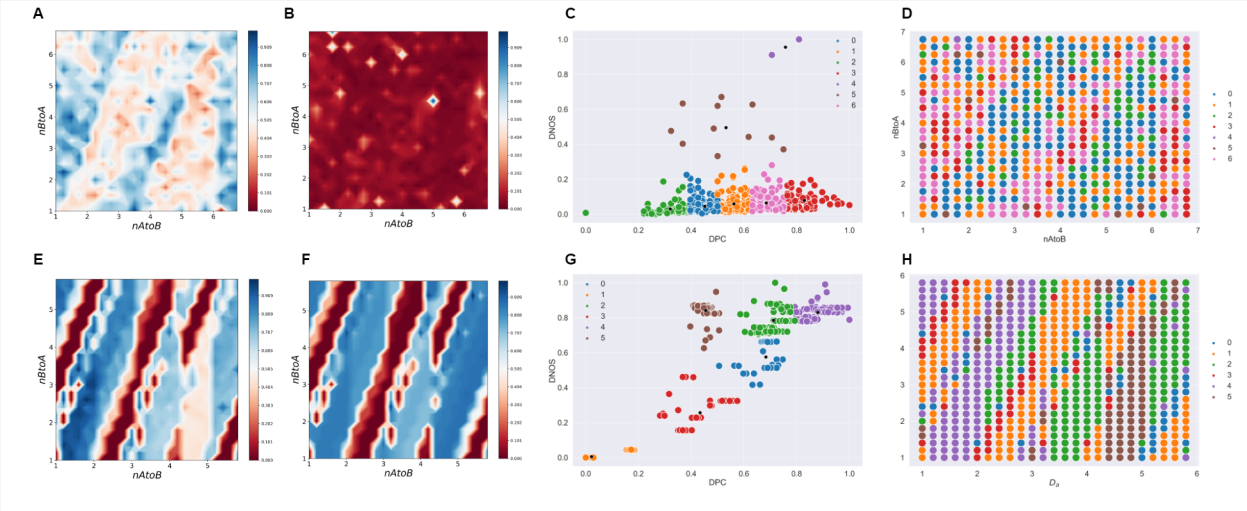

Figure 6: **Toggle switch models. A,B:** Normalised DPC and DNOS landscapes for the toggle switch with 2D diffusion. **C:** DPC–DNOS scatter with k-means clusters. **D:** Cluster assignments mapped back to the parameter grid. **E,F:** Normalised DPC and DNOS for the toggle switch with 2D diffusion and self-activation. **G:** DPC–DNOS scatter with k-means clusters for the self-activating system. **H:** Clusters mapped to parameter space.

Unlike the FitzHugh–Nagumo system, which is excitable and supports travelling pulses, the toggle-switch systems considered here produce stationary domain walls and pinned interfaces governed by bistability or tristability. These mechanistic differences lead to distinct structures in the $(\mathrm{DPC}, \mathrm{DNOS}, \mathrm{UME})$ feature space, despite superficial similarities in the visual appearance of some patterns.

2.7 The DNOS–DPC–UME complexity space

We next compare how different pattern-forming models populate the uniformity landscape defined by the Uniformity Measure of Entropy (UME) (Methods 5.3). UME plays a complementary role to DNOS and DPC in this summary representation. DNOS counts how many effective intensity states a model realises, and DPC reflects how structurally compressible the resulting spatial configurations are. UME does not duplicate either quantity: it measures how evenly the patterns produced by a model explore their available state or complexity range. When applied to state values (UME(S)), it reports whether intensity space is densely or sparsely occupied; when applied to compression ratios (UME(CR)), it describes whether the model generates a narrow or broad repertoire of structural complexities. By normalising entropy with $\log B$ and using the same bin resolution as DNOS, UME provides a consistent, dimensionless axis that allows different mechanistic models to be compared in a single computational space.

For each system we aggregate UME computed on (i) the distribution of per-pattern compression ratios (UME(CR), i.e. UME applied to DPC values; Methods 5.2), and (ii) the distribution of normalised state values across space (UME(S), i.e. UME applied to

intensity histograms; Methods 5.1). This yields one summary point per model in the $\big(\mathrm{UME(CR)}, \mathrm{UME}(S)\big)$ plane.

Figure 7 shows the resulting positions for the five systems studied in this work: the linearised Turing model (LINTP; Section 2.3), the Gray–Scott model (GSM; Section 2.4), the FitzHugh–Nagumo model (FHN; Section 2.5), the toggle switch with 2D diffusion (TGLS; Section 2.6.1), and the toggle switch with 2D diffusion and self-activation (TGLSWA; Section 2.6.2).

GSM, FHN, and TGLSWA cluster in the upper-right region of the plane, with UME(CR) $\approx$ 0.85 and UME(S) spanning roughly 0.5–1.0. This indicates that, for these systems, both the distribution of pattern complexities (DPC) and the underlying state intensities are relatively evenly spread across their available ranges. GSM, in particular, attains UME(S) ≈ 1, consistent with a nearly uniform exploration of intensity space. FHN and TGLSWA have slightly lower UME(S) values (~ 0.6 and ~ 0.5, respectively), reflecting high but not perfect uniformity of state distributions.

LINTP lies in the lower-right quadrant: it exhibits very high UME(CR) (close to 1), indicating that DPC values are evenly distributed across patterns, but only moderate UME(S) $\approx$ 0.45, suggesting more uneven usage of intensity space and hence greater variability in state diversity. In contrast, TGLS occupies the lower-left quadrant, with both UME(CR) and UME(S) close to zero. This is consistent with a system that generates comparatively simple, low-diversity patterns whose complexities and intensities are concentrated into a narrow subset of their possible ranges.

Taken together, this summary plot highlights how different mechanistic classes of pattern-forming PDEs (linear reaction–diffusion, autocatalytic, excitable, and GRN-based) occupy distinct regions of the $\big(\mathrm{UME(CR)}, \mathrm{UME}(S)\big)$ space. Models such as GSM, FHN, and TGLSWA exhibit high uniformity in both pattern complexity and state usage, whereas LINTP and especially TGLS are more restricted, underscoring how GRN architecture and nonlinearity shape the global organisation of pattern complexity across parameter space.

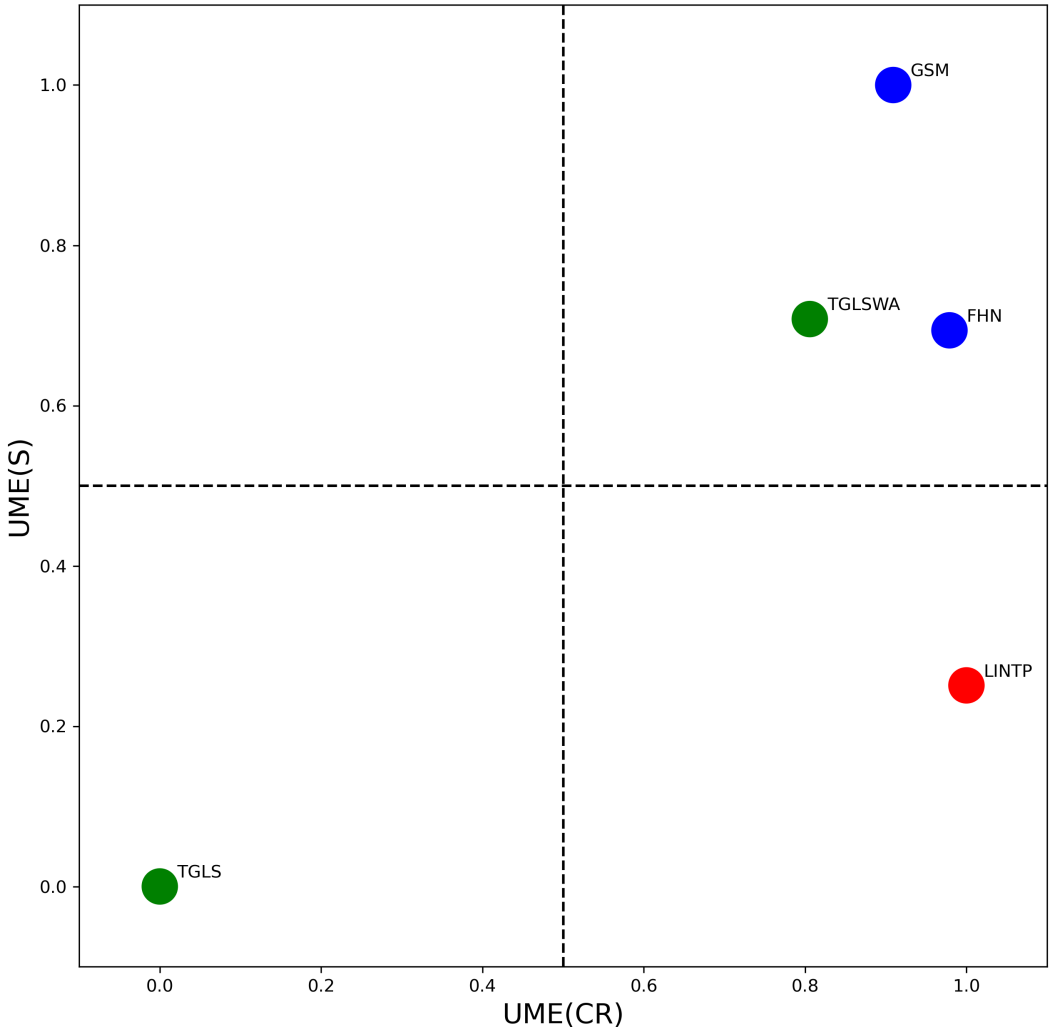

Figure 7: **Uniformity landscape across models.** Each point shows the Uniformity Measure of Entropy applied to compression ratios (UME(CR), horizontal axis) and to state values (UME(S), vertical axis) for one of the five models: linearised Turing (LINTP), Gray–Scott (GSM), FitzHugh–Nagumo (FHN), toggle switch with 2D diffusion (TGLS), and toggle switch with 2D diffusion and self-activation (TGLSWA). GSM, FHN, and TGLSWA occupy the upper-right region, indicating relatively uniform distributions of both pattern complexities and intensities (with GSM achieving nearly maximal UME(S)). LINTP shows high UME(CR) but only moderate UME(S), while TGLS lies near the origin, reflecting minimal uniformity in both complexity and state usage and thus a comparatively low-diversity pattern repertoire.

2.8 Notch, Delta, and EGF signalling in *Drosophila* neurogenesis

Neurogenesis in the *Drosophila* optic lobe provides a well studied example of how gene regulatory networks coordinate spatial patterning. Classical Notch–Delta lateral inhibition produces "salt-and-pepper" patterns during binary cell-fate decisions, but in the medulla a distinct travelling "proneural wave" propagates across the neuroepithelium. This wave is driven by proneural transcription factors (e.g. Lethal of scute) and is modulated by an EGF-mediated reaction–diffusion process that suppresses the usual lateral-inhibition pattern and instead establishes a coherent front of differentiation Sato et al. [2016]. In this system Notch does not directly impose a spatial alternation pattern: rather, EGF diffusion regulates the velocity and spatial organisation of Notch activation, highlighting a mode of GRN-based pattern formation that depends on reaction–diffusion coupling rather than static bistability alone.

We analyse the reaction–diffusion GRN model introduced in Sato et al. [2016], focusing on the four interacting fields: the EGF ligand E, the Notch receptor N, the Delta ligand D, and the proneural factor A. Their dynamics are governed by

$$\frac{\partial E}{\partial t} = d_e \nabla^2 E - k_e E + e_e E + n_e N + a_e A(A_0 - A) + \theta_E, \tag{13}$$

$$\frac{\partial N}{\partial t} = -k_n N + d_t \sum_{\text{neigh}} D - d_c D + \theta_N, \tag{14}$$

$$\frac{\partial D}{\partial t} = -k_d D + e_d E + a_d A(A_0 - A) + \theta_D, \tag{15}$$

$$\frac{\partial A}{\partial t} = e_a (A_0 - A) \max(E - N, 0) + \theta_A. \tag{16}$$

Here ∇^2 denotes the Laplacian; d_e is the only diffusing species (as in the experimental system), and the remaining interactions encode mutual reinforcement and inhibition between E, N, D, and A. Stochastic terms $\theta_{E,N,D,A}$ represent molecular noise.

To simulate mutant clones, individual regulatory interactions are set to zero exactly as in Sato et al. [2016]. For example, in EGF-deficient clones the self- and A-mediated activation of E (e_e, a_e) are suppressed; in Notch mutants the E→N and D→N terms are removed; and in Delta mutants E→D and A→D terms are removed (Table 4). This procedure isolates the contribution of each pathway to pattern formation.

We solve the PDE system using the finite-difference scheme described in Section 5.6. For each of three parameter sets (A, B, C) we simulate the wild-type system and the corresponding EGF, Notch, and Delta mutants. All simulations use a 20×20 spatial grid with 2000 iterations per run and 1000 random parameter samples per set. Parameter ranges for d_e, e_d, A_0, a_d, n_e, k_n, k_e, k_d, e_e, a_e, e_a, d_t, and d_c are summarised in Table 4. Outputs are analysed from the final snapshot only, after transients have decayed.

Table 4: Combined Parameter Settings for Proneural Wave Experiments

Parameter	**Set A**	**Set B**	**Set C**
d_e	[0.0, 1.0]	[0.0, 1.0]	Fixed at 1.0
e_d	[0.0, 1.0]	[0.0, 1.0]	Fixed at 1.0
A_0	[0.0, 1.0]	[0.0, 1.0]	Fixed at 1.0
n_e	[0.0, 1.0]	[0.0, 1.0]	[0.0, 2.0]
a_d	[0.0, 1.0]	[0.0, 1.0]	Fixed at 1.0
k_n	[0.0, 1.0]	[0.0, 1.0]	Fixed at 1.0
k_e	[0.0, 1.0]	[0.0, 1.0]	Fixed at 1.0
k_d	[0.0, 1.0]	[0.0, 1.0]	Fixed at 1.0
e_e	[0.0, 1.0]	[0.0, 1.0]	[0.0, 0.4]
a_e	[0.0, 1.0]	[0.0, 1.0]	[0.0, 2.0]
e_a	[0.0, 10.0]	[0.0, 10.0]	Fixed at 10.0
d_t	Fixed at 0.01	[0.0, 1.0]	[0.0, 0.5]
d_c	Fixed at 0.25	[0.0, 1.0]	[0.0, 0.5]

For each simulation we compute DNOS and DPC. All measures are computed using identical binning and normalisation across models. DNOS and DPC values are then min–max normalised within each parameter set to allow direct comparison across wild-type and mutant systems.

Figure 8 shows the resulting state-space plot of normalised DPC versus DNOS across all parameter sets and clone types. Wild-type points lie predominantly in the upper-right region, indicating both high pattern complexity and broad state diversity. Delta and EGF mutants shift markedly toward lower DNOS and lower DPC, reflecting strongly reduced pattern diversity and simpler spatial configurations. Notch mutants exhibit the most dramatic collapse, occupying the lower-left quadrant: both state diversity and pattern complexity are minimal, consistent with the biological role of Notch as a key regulator of wave propagation.

Together, the results show that the $(\mathrm{DNOS}, \mathrm{DPC})$ feature space provides a compact but informative summary of how GRN perturbations reshape pattern formation in this developmental system, capturing the distinctions between reaction–diffusion-driven wave propagation (wild type), disrupted wave fronts (EGF mutant), impaired lateral signalling (Delta mutant), and complete failure of organised patterning (Notch mutant).

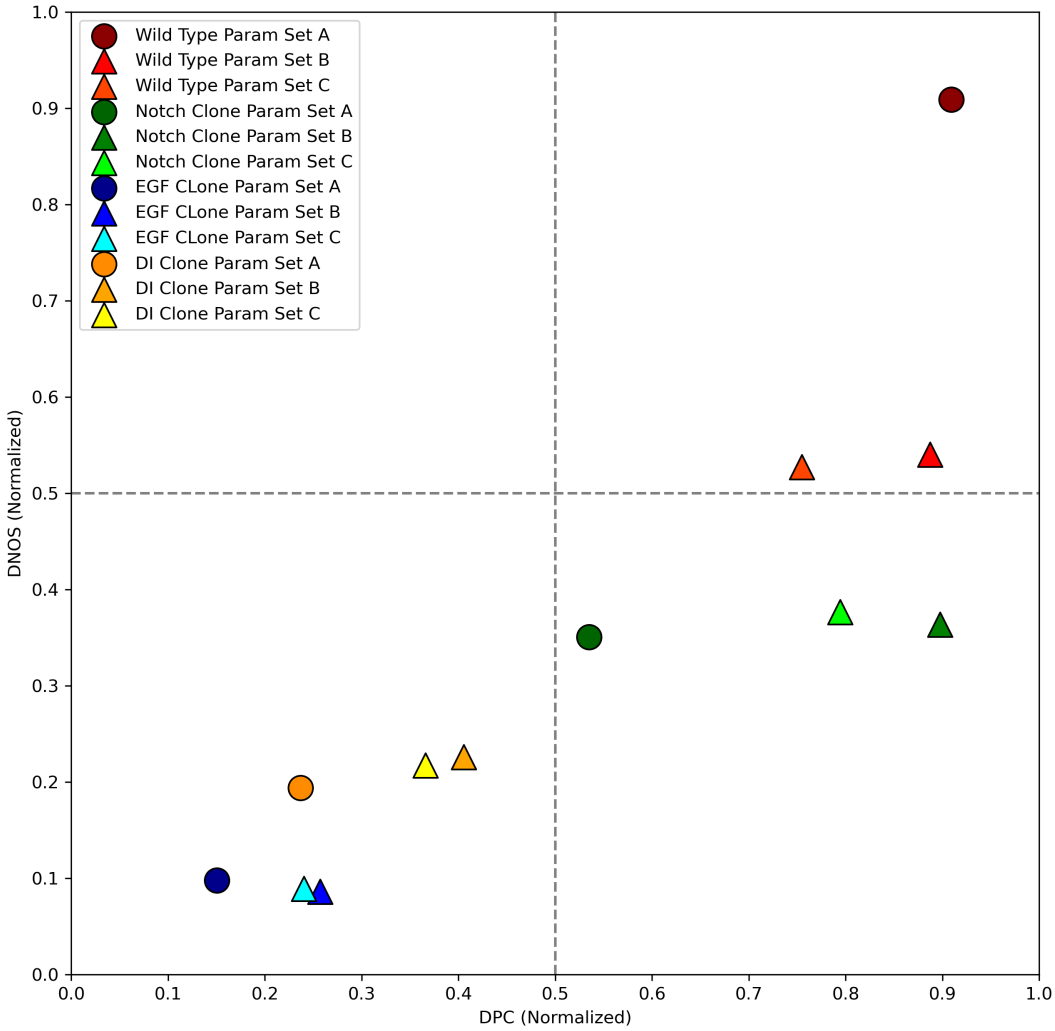

Figure 8: **Pattern–complexity landscape in Notch–Delta–EGF signalling.** Normalised pattern–compression complexity (DPC) plotted against the normalised diversity of number of states (DNOS) for wild type and EGF, Notch, and Delta mutant simulations. Points are colour–coded by clone type and marker shapes indicate the three parameter sets (A–C). Dashed lines at 0.5 on both axes divide the space into four regions. Wild–type simulations cluster in the high–complexity and high–diversity quadrant, whereas all mutants shift toward lower DPC and DNOS values, consistent with reduced spatial organisation in the underlying signalling network.

3 Discussion

This work develops a quantitative framework for comparing spatial patterns generated by reaction–diffusion systems and gene regulatory networks. The measures DNOS, DPC, and UME are used to summarise how many intensity states appear in a pattern, how compressible the pattern is, and how uniformly the intensity range is occupied. These measures provide

a compact description that does not depend on geometric labels such as spots or stripes.

Classical linear stability analysis identifies when a homogeneous steady state becomes unstable, but it does not describe the nonlinear pattern that finally emerges or the degree of complexity in that pattern. Across the examples considered here, the joint organisation of DNOS, DPC, and UME reveals structure in parameter space that is not visible from the linear theory alone. In the linearised reaction–diffusion system, specific regions of the diffusion parameter plane consistently produce patterns with higher or lower DNOS and DPC values, indicating differences in both state diversity and structural detail.

For the nonlinear systems (Gray–Scott, FitzHugh–Nagumo, and the toggle-switch models), DNOS and DPC separate parameter space into regions associated with distinct behaviour. High DPC values occur where the models produce self-replicating structures, labyrinths, oscillatory fronts, or multiple domains. Low DPC values correspond to more homogeneous or weakly organised states. The measures therefore offer a concise way to compare systems whose patterns differ widely in visual appearance.

We compared DPC with several established descriptors (RDH, ESP, and WLE) to assess how it relates to existing measures of pattern irregularity. DPC shows strong agreement with RDH and WLE, which reflect topological and multiscale detail, and weaker agreement with ESP, which reflects spectral energy. This suggests that DPC captures structural detail that is similar to several classical descriptors while also containing information not fully represented by them.

DNOS plays a complementary role. At high resolution it is sensitive to fine-scale occupancy of intensity space, including subthreshold variation and interface structure. UME distinguishes patterns that occupy the intensity range evenly from those that concentrate values in narrow intervals. Taken together, DNOS, DPC, and UME provide a low-dimensional summary of how a system uses its available state space and how those states are arranged in the spatial domain.

The gene-regulatory models illustrate how this type of quantitative description connects to biological interpretation. Parameter regimes that include self-activation in toggle-switch systems produce increased DNOS and DPC, consistent with the additional states expected from positive feedback. In the Notch–Delta–EGF system, shifts in DNOS and DPC under mutant conditions match the expected reductions in the propagation and organisation of the proneural wave.

These observations indicate that DNOS and DPC can help summarise how reaction–diffusion and regulatory systems respond to changes in parameters, network structure, or external signals. They do not replace geometry-specific analyses or mechanistic models, but they offer a complementary and model-independent way to compare pattern-forming behaviour.

Future extensions might include applications to multicomponent fields, time-dependent trajectories, or three-dimensional domains, as well as a closer connection to bifurcation analysis and data-driven methods. Within the present scope, DNOS, DPC, and UME place a wide range of patterns in a common quantitative space and allow their organisation to be examined across different models and parameter regimes.

4 Methods

4.1 Numerical methods and stability checks

All nonlinear reaction–diffusion systems in this study are simulated on a rectangular grid using a standard five-point finite-difference discretisation of the Laplacian with grid spacing Δx and an explicit time-stepping scheme with time step Δt. Unless stated otherwise, we impose Neumann (zero-flux) boundary conditions, which preserve mass in the absence of reaction terms. For each model we choose $(\Delta x, \Delta t)$ such that the linear Courant–Friedrichs–Lewy (CFL) condition for the diffusion operator is satisfied with a safety factor of at least 2.

Reaction terms are evaluated pointwise. In models whose state variables represent non-negative concentrations, any numerically induced small negative values are truncated to 0 to prevent unphysical drift.

For each parameter set we initialise the fields at their homogeneous steady state plus small-amplitude Gaussian noise, and integrate to a final time T_{final} at which the spatial patterns have saturated. All complexity measures (DNOS, DPC, UME) are computed from the final snapshot only; we do not perform temporal averaging or interpolation. Hence all complexity landscapes shown in the paper are based on the stationary patterns produced by the nonlinear PDEs rather than transient trajectories.

To verify that the reported results are not numerical artefacts, we performed systematic resolution checks. For representative parameter sets in each model we repeated simulations with Δx and Δt halved, keeping the domain size and final time fixed. Spatial intensity statistics (histograms, DNOS, UME) and compression-based complexity (DPC) changed by less than 1%, and the locations of regime boundaries in the $(\text{DPC}, \text{DNOS}, \text{UME})$ space were unchanged.

We further validated the diffusion operator by comparing numerical eigenvalues of the discrete Laplacian with the analytical spectrum on test fields. Together, these checks demonstrate that the complexity measures and regime structure we report arise from the underlying PDE dynamics rather than from discretisation or numerical artefacts.

We emphasise that all complexity measures reported in this work (DNOS, DPC, UME) are computed from fully nonlinear reaction–diffusion models (Gray–Scott, FitzHugh–Nagumo, toggle switch, proneural wave), simulated to a saturated pattern and normalised to $[0, 1]$ prior to analysis. The linearised reaction–diffusion system is used only for dispersion-relation calculations and classification of stability and bifurcation types; we do not integrate the linearised PDE in time nor use it directly for complexity measurements.

4.2 Turing Model Stability Analysis

In this section we analyse the linear stability of a generic two-species reaction–diffusion system by linearising the kinetics around a homogeneous steady state and studying the resulting dispersion relation. This linearised reaction–diffusion system is used solely as an analytic tool to map stability and bifurcation structure in parameter space; pattern simulations and complexity measures are based on the corresponding nonlinear PDEs described below.

The inherent nonlinear nature of the reaction functions $f(u, v)$ and $g(u, v)$ is often simplified through linearization around an equilibrium point (u_0, v_0):

$$
\begin{aligned}
f(u,v) &\approx f(u_0,v_0) + \frac{\partial f}{\partial u}(u_0,v_0)(u-u_0) + \frac{\partial f}{\partial v}(u_0,v_0)(v-v_0), \\
g(u,v) &\approx g(u_0,v_0) + \frac{\partial g}{\partial u}(u_0,v_0)(u-u_0) + \frac{\partial g}{\partial v}(u_0,v_0)(v-v_0).
\end{aligned} \tag{17}
$$

This simplifies the original nonlinear reaction-diffusion equations to a set of linear PDEs.

Applying this to our linearised reaction–diffusion system and if the diffusion terms are ignored, it is easy to show that this system has only one equilibrium point $(u0 = h, v0 = k)$. This equilibrium point can be stable for many parameter values for a,b,c, and d. However, introducing spatial dimensions and diffusion terms to the equations may destabilize the equilibrium, and thus the system may spontaneously self-organize into a non-homogeneous pattern. We can relate the constants a, b, c, and d to the partial derivatives of the reaction functions at the equilibrium point: $a = \frac{\partial f}{\partial u}(u_0, v_0)$, $b = \frac{\partial f}{\partial v}(u_0, v_0)$, $c = \frac{\partial g}{\partial u}(u_0, v_0)$, and $d = \frac{\partial g}{\partial v}(u_0, v_0)$.

One can now convert the PDE equations into a matrix equation describing the system is given by:

$$
A = \begin{bmatrix} a & b \\ c & d \end{bmatrix} \tag{18}
$$

$$
\mathcal{D} = det(A) \tag{19}
$$

$$
\mathcal{T} = Tr(A) \tag{20}
$$

$$
\lambda \begin{bmatrix} \hat{u}(k) \\ \hat{v}(k) \end{bmatrix} = \begin{bmatrix} a - D_u k^2 & b \\ c & d - D_v k^2 \end{bmatrix} \begin{bmatrix} \hat{u}(k) \\ \hat{v}(k) \end{bmatrix} \tag{21}
$$

One can now find the eigenvalues of the matrix A by considering the characteristic equation of the matrix:

$$
\det(\mathbf{A} - \lambda \mathbf{I}) = \lambda^2 - \lambda \mathcal{T}^2 + \mathcal{D} \tag{22}
$$

and by finding the solutions of the quadratic equation:

$$
\lambda_{1,2} = \frac{1}{2}\left(\mathcal{T} \pm \sqrt{\mathcal{T}^2 - 4\mathcal{D}}\right) \tag{23}
$$

Based on the nature of the derived eigenvalues one can infer when the system is stable against small perturbation and when it is unstable. Here are the main cases:

We consider various stability cases:

I. Stability and Instability

1. Stable Fixed Point: Both eigenvalues have negative real parts.
   - $\lambda_1 < 0$ and $\lambda_2 < 0$

2. Unstable Fixed Point: At least one eigenvalue has a positive real part.
   - $\lambda_1 > 0$ or $\lambda_2 > 0$

II. Saddle Points

1. A saddle point occurs when one eigenvalue has a positive real part, and the other has a negative real part.
   - $\lambda_1 > 0$ and $\lambda_2 < 0$

2. $\lambda_1 < 0$ and $\lambda_2 > 0$

III. Bifurcations

1. Bifurcations occur when one or both eigenvalues cross zero as a parameter varies, leading to qualitative changes in the system's behavior.

Transcritical Bifurcation: One eigenvalue passes through zero as a parameter changes.
   - $\lambda_1 = 0$ or $\lambda_2 = 0$

Pitchfork Bifurcation: Both eigenvalues simultaneously pass through zero as a parameter changes.
   - $\lambda_1 = \lambda_2 = 0$

IV. Hopf Bifurcation

Hopf bifurcation occurs when the eigenvalues become purely imaginary, giving rise to oscillatory behavior.
This requires the discriminant of the characteristic equation to be zero:
   - $(a + d - D_u k^2 - D_v k^2)^2 - 4(ad - bc - D_u D_v k^4 + (aD_v + dD_u)k^2) = 0$

The stability and instability regions, fixed points, and bifurcations can be found by analyzing the eigenvalues and discriminant for different combinations of parameters and the wave vector k. Due to the complexity of the stability analysis, numerical methods are commonly employed to determine the stability and instability regions, fixed points, and bifurcations. By systematically varying the parameters and wave vector k, one can numerically solve the characteristic equation and compute the eigenvalues. These results can then be used to identify different stability cases and investigate the behavior of the system under specific conditions.

Given the Jacobian matrix for a Turing pattern system,

$$J = \begin{pmatrix} a - D_a k^2 & b \\ c & d - D_b k^2 \end{pmatrix}, \tag{24}$$

where a, b, c, and d are system parameters, D_a and D_b are the diffusion coefficients, and k is the wave number.

The characteristic equation, or dispersion relation, ω is given by,

$$\omega = \mathrm{Tr}(J) + \sqrt{\mathrm{Tr}(J)^2 - 4\mathrm{Det}(J)}, \tag{25}$$

which simplifies to,

$$\omega = a + d - (D_a + D_b)k^2 + \sqrt{4bc + (a - d - D_a k^2 + D_b k^2)^2}. \tag{26}$$

Differentiating ω with respect to k^2, we obtain,

$$\frac{d\omega}{dk^2} = -D_a - D_b + \frac{(-D_a + D_b)(a - d + (-D_a + D_b)k^2)}{\sqrt{4bc + (a - d + (-D_a + D_b)k^2)^2}}. \tag{27}$$

Solving $\frac{d\omega}{dk^2} = 0$ for k^2, we find,

$$k^2 = \frac{(a - d)D_a(D_a - D_b)D_b \pm \sqrt{-bcD_aD_b(D_a^2 - D_b^2)^2}}{D_a(D_a - D_b)^2 D_b}. \tag{28}$$

This solution gives the values of k^2 at which the growth rate ω reaches its extremum, indicating the scale of Turing patterns for given system parameters.

The characteristic length scale L of emergent Turing patterns is inversely related to the dominant wavenumber k_{dom}, where the growth rate $\lambda(k)$ is maximized. To determine k_{dom}, we perform the following steps:

First, maximize the growth rate by setting the derivative with respect to k^2 to zero:

$$\frac{d\lambda}{dk^2} = -(D_a + D_b) + \frac{(-D_a + D_b)(a - d - (D_a - D_b)k^2)}{\sqrt{4bc + (a - d - (D_a - D_b)k^2)^2}} = 0.$$

This quadratic equation in k^2 is solved numerically to obtain critical wavenumbers k_1^2 and k_2^2, retaining only real and positive solutions.

Next, select the dominant wavenumber as the larger of the valid solutions:

$$k_{\mathrm{dom}} = \max(k_1^2, k_2^2).$$

Finally, compute the pattern length scale using:

$$L = \frac{2\pi}{k_{\mathrm{dom}}}.$$

This relation indicates that the spatial periodicity of the Turing pattern is inversely proportional to the dominant wavenumber, providing a quantitative measure of the pattern's characteristic size.

5 Complexity Measures

A central aim of this work is to quantify how reaction–diffusion partial differential equations (PDEs) explore and encode complexity across parameter space. Rather than classifying patterns by their geometric phenotype (e.g. "spots" vs. "stripes"), we adopt a computational perspective: a PDE is treated as a dynamical information-processing system, and the emergent spatial fields are analysed by measures that reflect (i) the breadth of representable states, (ii) the compressibility of patterns, and (iii) the uniformity of encoded information. This section describes the three complementary measures used throughout the paper: the Differential Number of States (DNOS), the Discrete Pattern Complexity (DPC), and the Uniformity Measure of Entropy (UME). All measures operate directly on simulated fields and require no geometric feature extraction.

To obtain robust statistics while covering the parameter space, we stratify the grid of parameter settings into five non-overlapping *pools*. From each pool we draw up to 40 representative patterns (typically the last snapshots of independent PDE realisations) and compute all measures per image independently. Unless stated otherwise, figures report *pooled* quantities: for a given pool we average a measure across its images, and then report the distribution of these pool-level means.

5.1 Diversity Number of States (DNOS)

Let $X(\mathbf{x})$ denote a normalised concentration field with values in $[0, 1]$ on a regular pixel grid. Classical discretised state-counting measures depend strongly on the number of bins B used to histogram intensities. In our implementation we therefore distinguish between (i) a simple *occupied-bin* DNOS, which is the primary quantity used throughout the paper, and (ii) an *entropy-based* DNOS and its bin-free limit, which we use as diagnostic checks to verify that the occupied-bin statistic is consistent with standard information-theoretic diversity measures.

Operational DNOS: occupied-bin count. For a fixed bin count B we partition the normalised range $[0, 1]$ into B equal-width intervals and compute the empirical histogram of intensities. Let p_i denote the fraction of pixels falling into bin i. Our operational DNOS at resolution B is then defined as the number of non-empty bins,

$$\mathrm{DNOS}_{\mathrm{occ}}(B) = \big|\{\, i \in \{1, \ldots, B\} : p_i > 0 \,\}\big|. \tag{29}$$

Intuitively, $\mathrm{DNOS}_{\mathrm{occ}}(B)$ counts how many intensity intervals are actually used by the pattern at the chosen resolution. For all models and parameter sets we use the same set of B bins, defined as equal-width intervals partitioning the normalised range $[0, 1]$; no adaptive binning or data-dependent edges are used.

In all regime-identification analyses we fix a high bin count B^* in the sparse-histogram regime (here $B^* = 512$ unless stated otherwise) and use $\mathrm{DNOS}_{\mathrm{occ}}(B^*)$ as the DNOS coordinate in feature space. Patterns that concentrate intensity into a narrow range (high contrast, strong saturation) populate fewer fine-scale bins and therefore have smaller $\mathrm{DNOS}_{\mathrm{occ}}(B^*)$, whereas patterns with more broadly distributed intensities retain a larger $\mathrm{DNOS}_{\mathrm{occ}}(B^*)$.

We stress that a coarse, low-resolution DNOS (small B) behaves like a simple count of occupied grey levels and is not intended to distinguish different geometries with the same coarse palette (e.g. two distinct binary patterns will both have $\mathrm{DNOS}_{\mathrm{occ}}(B) = 2$ for $B = 2$). At high resolution, however, $\mathrm{DNOS}_{\mathrm{occ}}(B^*)$ becomes sensitive to fine-scale occupancy of intensity space, including small sub-threshold fluctuations, interface thickness, and multimodal clustering of values. Patterns with similar coarse palettes but different fine-scale structure (e.g. smooth gradients versus sharply segregated domains) therefore have markedly different $\mathrm{DNOS}_{\mathrm{occ}}(B^*)$.

Entropy-based DNOS and bin-free reference. To relate the occupied-bin DNOS to continuous notions of diversity, and to assess sensitivity to the choice of B, we also compute an entropy-based surrogate and its bin-free limit. Given the same histogram probabilities p_i, the discrete Shannon entropy is

$$H_B = -\sum_{i=1}^{B} p_i \log p_i, \qquad \mathrm{DNOS}_{\mathrm{ent}}(B) = \exp(H_B). \tag{30}$$

In addition, we estimate a smooth intensity distribution $\hat{p}(x)$ on $[0, 1]$ using a boundary-corrected kernel density estimator (KDE) with automatic bandwidth selection, and define the continuous Hill-entropy diversity

$$D_1 = \exp(H(\hat{p}))\,, \qquad H(\hat{p}) = -\int_0^1 \hat{p}(x) \log \hat{p}(x)\, dx. \tag{31}$$

To study convergence with B we evaluate $\mathrm{DNOS}_{\mathrm{ent}}(B)$ on a grid of bin counts $B \in \{32, 64, 128, 256, 512, 1024\}$. For each pool and each B we compute $\mathrm{DNOS}_{\mathrm{ent}}(B)$ per image, average across images, and finally average across the five pools. Figure 9 shows the resulting pooled mean and ± 1 standard deviation across pools. For $B \leq 128$, $\mathrm{DNOS}_{\mathrm{ent}}(B)$ lies on a plateau that agrees, within sampling error, with the bin-free reference $D_1 = \exp(H(\hat{p}))$. This dense-histogram regime confirms that coarse-graining does not affect the qualitative organisation of complexity regimes and that the discrete and continuous definitions of DNOS are consistent. For larger B (here $B \geq 256$), the histograms enter a *sparse* regime in which many bins contain zero or one count and both $\mathrm{DNOS}_{\mathrm{ent}}(B)$ and $\mathrm{DNOS}_{\mathrm{occ}}(B)$ become explicitly resolution-dependent. In this regime we deliberately fix B^* and treat DNOS as a resolution-dependent occupancy measure, using $\mathrm{DNOS}_{\mathrm{occ}}(B^*)$ as the domain-separating feature reported in the main text.

5.2 Discrete Pattern Complexity (DPC)

To quantify structural complexity of patterns, we measure their algorithmic compressibility, following ideas from Kolmogorov complexity and practical coding-based estimators Li and Vitányi [2008], Vitányi [2021]. For an image I, we compute the length of its gzip-compressed byte string, normalized by the raw size:

$$\mathrm{DPC}(I) = \frac{|\mathrm{gzip}(I)|}{|I|}. \tag{32}$$

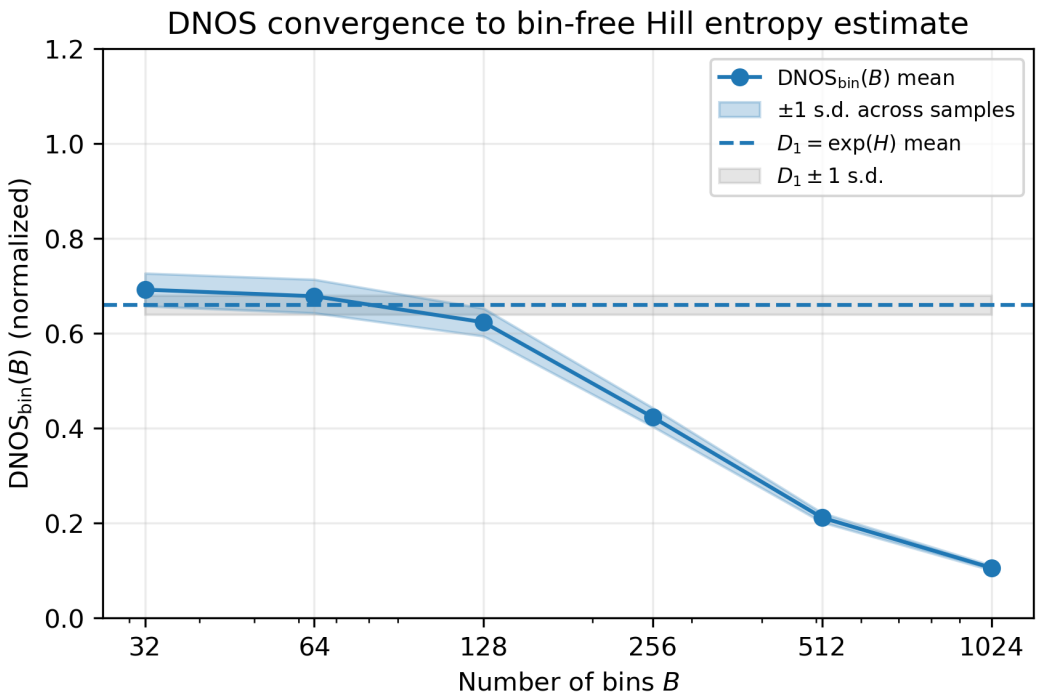

Figure 9: **Entropy-based DNOS and bin-free reference.** Mean and ±1 s.d. of the entropy-based DNOS $\mathrm{DNOS}_{\mathrm{ent}}(B) = \exp(H_B)$, pooled over five parameter-space samples, as a function of histogram bin count B (solid curve and blue band). The dashed line denotes the bin-free Hill-entropy estimate $D_1 = \exp(H(\hat{p}))$, with grey band indicating ±1 s.d. across pools. For moderate B the discrete DNOS agrees with D_1 (dense-histogram regime), while for large B the histogram becomes sparse and $\mathrm{DNOS}_{\mathrm{ent}}(B)$ transitions into a resolution-dependent occupancy measure. In the main analyses we use the occupied-bin DNOS $\mathrm{DNOS}_{\mathrm{occ}}(B^*)$ at a fixed high resolution B^*, whose qualitative ordering is consistent with the behaviour of $\mathrm{DNOS}_{\mathrm{ent}}(B)$ in this regime.

This yields a scalar complexity score per pattern, where low values correspond to high compressibility (regular or nearly homogeneous patterns) and high scores correspond to algorithmically rich, less compressible structures.

To assess robustness, we recomputed DPC using three independent codecs (lzma, bz2, and PNG encoding) and compared per-image scores within each pool. For every pool and every codec pair we computed the Spearman rank correlation between DPC values, and then averaged these correlations across the five pools (Fig. 10). For all codec pairs, mean rank correlations exceeded $\rho > 0.98$ with small across-pool variance, and regime boundaries in the $(\mathrm{DPC}, \mathrm{DNOS})$ feature plane remained unchanged. This demonstrates that the complexity ordering is intrinsic to the patterns and not an artefact of a particular compression algorithm.

Throughout, each image is compressed independently; DPC is therefore a per-pattern complexity score. Aggregating DPC across parameter sets yields a distribution over complexity levels, but the definition itself does not depend on any temporal ordering of patterns.

We also assessed robustness to observational noise by adding independent Gaussian perturbations with standard deviation $\sigma \in [10^{-3}, 10^{-2}]$ to each pixel and recomputing DPC with

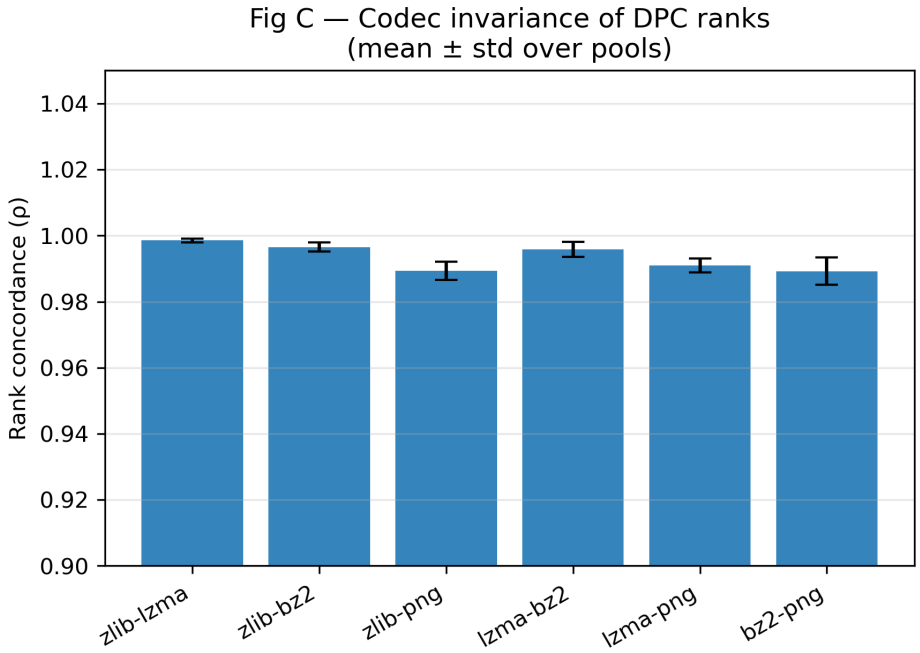

Figure 10: **Compressor invariance of DPC.** Mean ± s.d. of Spearman rank correlations between per-image DPC scores computed with different codecs (gzip, lzma, bz2, PNG), aggregated over five parameter-space pools. High concordance ($\rho \gtrsim 0.98$ for all pairs) demonstrates that the DPC ordering is intrinsic to the patterns and not an artefact of codec choice.

each codec. Across all models and parameter-space pools, the Spearman rank correlation of per-pattern DPC values between noisy and noise-free images remained above $\rho > 0.97$, indicating that the DPC ordering is stable under modest image noise.

To situate DPC within the broader family of quantitative pattern descriptors, we further compared DPC scores with three commonly used measures of spatial structure: (i) a resistance–distance histogram (RDH) derived from a graph-based representation of the pattern; (ii) Fourier-domain spectral energy (ESP); and (iii) the wavelet energy ratio (WLE) obtained from biorthogonal wavelet decompositions (definitions given in Secs. 5.5.1–5.5.3). For each image and each measure we computed pairwise Pearson correlation coefficients and mean-squared error (MSE) between the normalised complexity landscapes across the (D_u, D_v) parameter plane. These statistics were averaged across the five parameter-space pools. The resulting correlation and MSE heatmaps for the Gray–Scott and FitzHugh–Nagumo models are shown in panels E of Figs. 4 and 5. DPC shows consistently high concordance with RDH and WLE (typical Pearson correlations $\rho \approx 0.85$–0.95) and moderate correlation with ESP ($\rho \approx 0.25$–0.45), indicating that DPC captures structure that overlaps with,but is not reducible to,existing graph-based, spectral, or wavelet descriptors. These comparisons demonstrate that DPC behaves as an interpretable global complexity measure aligned with multiple classical metrics while remaining mathematically simple, model-agnostic, and compressor-invariant.

5.3 Uniformity Measure of Entropy (UME)

The UME quantifies how uniformly a pattern uses its available intensity space. Given the binned intensity distribution over B equally spaced bins,

$$p_i = \frac{\text{count in bin } i}{\sum_j \text{count in bin } j}, \tag{33}$$

the UME is defined as

$$\mathrm{UME}(I) = \frac{-\sum_{i=1}^{B} p_i \log p_i}{\log B}. \tag{34}$$

UME attains 1 for perfectly uniform distributions and 0 when all mass concentrates into a single bin.

In practice we use the same high-resolution bin count B^* and the same uniform bin edges on $[0, 1]$ as for $\mathrm{DNOS}_{\mathrm{bin}}(B^*)$, ensuring that DNOS and UME probe intensity statistics at a common scale. This joint use of sparse-regime DNOS and UME allows smooth intensity gradients (high UME, lower sparse-regime DNOS) to be distinguished from sharply segregated, multi-domain patterns (lower UME, higher sparse-regime DNOS), even when their coarse intensity histograms are similar.

For each pool we compute the mean DPC, the mean bin-free DNOS D_1, and the mean UME across its images. Figure 11 overlays these pooled feature values: at a given pooled DPC (horizontal coordinate), blue points denote the corresponding pooled D_1 and orange points the pooled UME. UME rescales and compresses the vertical axis while preserving the DPC ordering, providing a more stable and separable measure of how intensity space is used.

Although UME is expressed using the Shannon entropy of a binned distribution, it is not used here as a general-purpose information measure. Its role is to provide a controlled, model-independent normalisation that links DNOS and DPC on a common intensity scale. Classical entropy describes uncertainty in an abstract probability distribution, whereas UME is always computed on two specific empirical distributions generated by our framework: the binned spatial intensities of a pattern and the binned per-pattern compression ratios.

Because UME uses the same bin edges and resolution as $\mathrm{DNOS}_{\mathrm{bin}}(B^*)$, both measures probe intensity space consistently, with DNOS counting which bins are occupied and UME quantifying how evenly those occupied bins are filled. Normalisation by $\log B$ removes dependence on the absolute bin count and on the different dynamic ranges of the underlying models. In this role UME provides information that Shannon entropy alone cannot supply: it situates DNOS and DPC within a common, dimensionless scale and compares patterns across reaction–diffusion systems and gene regulatory networks without requiring system-specific geometric assumptions.

5.4 Regime Identification via Probabilistic Partitioning

We identify computational regimes by fitting Gaussian Mixture Models (GMMs) in the multidimensional feature space composed of

$$\big(\mathrm{DPC},\ \mathrm{DNOS}_{\mathrm{bin}}(B^*),\ \mathrm{UME}\big),$$

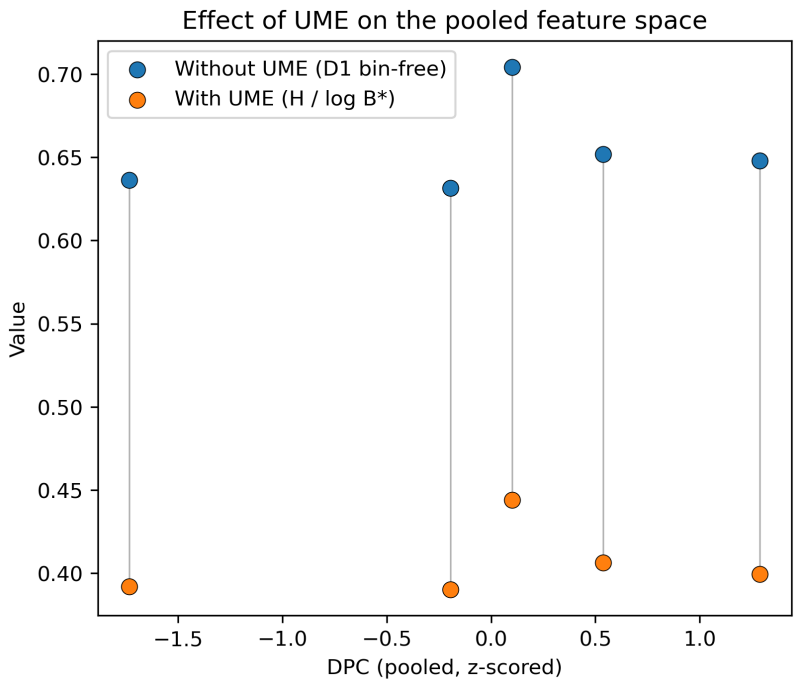

Figure 11: **Effect of UME on the pooled complexity feature space.** Each point corresponds to one parameter-space pool. Horizontal position is pooled DPC (z-scored); vertical position is either the pooled bin-free DNOS D_1 (blue) or the pooled UME (orange) computed from the same images. UME compresses the dynamic range of the vertical axis while preserving the horizontal ordering, yielding a more stable and separable complexity landscape.

after z-scaling each component. The feature vectors used for clustering are computed per image; regime assignments are then analysed both at the image level and after pooling over parameter-space samples. The bin-free DNOS D_1 is used as a diagnostic only, to verify that discrete DNOS behaves consistently with the underlying continuous entropy; the actual partitioning across parameter space is driven by the sparse-regime DNOS $\mathrm{DNOS}_{\mathrm{bin}}(B^*)$ together with DPC and UME. The number of regimes is selected by Bayesian Information Criterion (BIC), and stability is quantified by silhouette score and Davies–Bouldin index. Across random subsampling of patterns, across choices of $B^* \in \{256, 512, 1024\}$, and across the five parameter-space pools, regime boundaries remain stable (ARI > 0.9; NMI > 0.9), demonstrating that the inferred complexity landscape is robust to sampling noise and to the particular resolution at which DNOS is evaluated.

We therefore interpret the resulting mixture components as statistically stable computational regimes in the $(\mathrm{DPC}, \mathrm{DNOS}_{\mathrm{bin}}(B^*), \mathrm{UME})$ space, rather than as a one-to-one labelling of visually defined pattern types.

This integrative framework provides a principled, reproducible, and compressor-invariant quantification of pattern complexity in reaction–diffusion systems. Together, DNOS, DPC, and UME reveal coherent computational regimes that emerge directly from the PDE dynamics, independent of visual taxonomy.

5.5 Auxiliary Complexity Measures for Benchmarking DPC

To benchmark DPC against established notions of spatial complexity, we also compute three auxiliary descriptors that are widely used in image and pattern analysis but are *not* used to define regimes: (i) Fourier-domain spectral energy (ESP), (ii) a resistance–distance histogram (RDH) derived from a graph-based representation of the pattern, and (iii) a wavelet energy ratio (WLE) based on biorthogonal wavelet decompositions. Their definitions are given below. These measures are used solely in correlation and error analyses (Figs. 4E and 5E) to assess how DPC relates to more traditional graph-, spectral-, and wavelet-based descriptors of pattern structure.

5.5.1 Spectral Energy

For an image represented by a matrix $\mathbf{I} \in \mathbb{R}^{m\times n}$, the spectral energy E_{spectral} quantifies the total energy of its frequency components, excluding the zero frequency. This is computed by first applying the two-dimensional discrete Fourier transform (DFT):

$$\mathbf{F}(u,v) = \sum_{x=0}^{m-1}\sum_{y=0}^{n-1} \mathbf{I}(x,y)\, e^{-2\pi i\left(\frac{ux}{m}+\frac{vy}{n}\right)},$$

for each spatial frequency (u,v). The zero-frequency component is excluded by setting $\mathbf{F}(0,0) = 0$. The spectral energy is then calculated as the sum of the squared magnitudes of the Fourier coefficients:

$$E_{\text{spectral}} = \sum_{u=0}^{m-1}\sum_{v=0}^{n-1} \left|\mathbf{F}(u,v)\right|^2,$$

where $|\mathbf{F}(u,v)|$ denotes the magnitude of the complex Fourier coefficients.

The spectral energy E_{spectral} measures the total power of the image's frequency content, emphasizing variations such as edges and textures. A higher E_{spectral} indicates greater complexity and richness in high-frequency components, corresponding to intricate patterns within the image. In this work, ESP is used as an auxiliary comparator for DPC rather than as a primary regime-defining feature.

5.5.2 Resistance Distance Histogram

For an image represented by a concentration matrix $\mathbf{C} \in \mathbb{R}^{n\times n}$, a graph $G(V,E)$ is constructed where each C_{ij} maps to a vertex v_{ij} in V. Edges (v_{ij}, v_{kl}) are formed between vertices within a neighbourhood radius r if the associated concentration values meet the condition $(C_{ij} \geq \theta \wedge C_{kl} \geq \theta) \vee (C_{ij} < \theta \wedge C_{kl} < \theta)$, where θ is the mean concentration if not specified. Edges are weighted 1 if the condition is met, otherwise a small value ϵ is used.

Graph G may be optionally undersampled by a factor t, reducing the number of vertices and edges to simplify the computational requirements. Resistance distances in G are calculated by first constructing the weighted adjacency matrix Ω_G. The graph Laplacian $\mathbf{L}_G = \mathbf{D}_G - \Omega_G$ is then formed, where $\mathbf{D}_G$ is the degree matrix with entries equal to the sum of the edge weights for each vertex. The resistance distance matrix $\mathbf{R}$ is derived from the pseudoinverse $\mathbf{K}$ of $\mathbf{L}_G$, calculated as $R_{ij,kl} = K_{ii} + K_{ll} - 2K_{il}$.

The histogram of resistance distances is computed by binning $\mathbf{R}$ into a pre-defined number of bins within the range $[0, R_{\max}]$ and normalizing the histogram so that the sum of its values equals one, assuming the sum is non-zero. As with ESP, RDH is used here as a benchmark comparator for DPC and not as a primary feature in the regime-identification pipeline.

5.5.3 Wavelet Energy Ratio

Given an image matrix $\mathbf{A} \in \mathbb{R}^{x \times y}$, the wavelet energy ratio is computed using the biorthogonal wavelet 'bior1.3'. The two-dimensional discrete wavelet transform of $\mathbf{A}$ yields four sets of coefficients: approximation coefficients cA, horizontal detail coefficients cH, vertical detail coefficients cV, and diagonal detail coefficients cD. The energies of the detail and approximation components are calculated by summing the squares of their respective coefficients:

$$E_{\text{detail}} = \sum(cH^2) + \sum(cV^2) + \sum(cD^2), \qquad E_{\text{approximation}} = \sum(cA^2).$$

If the approximation energy $E_{\text{approximation}}$ is non-zero, the wavelet energy ratio R is defined as the ratio of the detail energy to the approximation energy:

$$R = \frac{E_{\text{detail}}}{E_{\text{approximation}}}.$$

If $E_{\text{approximation}} = 0$, R is set to zero. This metric quantifies the relative energy content in the detailed versus smoothed components of the image and, as with ESP and RDH, is used here as a benchmark comparator for DPC rather than as a primary regime-defining feature.

5.6 Numerical Simulation of the Turing Patterns PDE

Turing patterns emerge in reaction-diffusion systems, which are typically modeled by a set of coupled partial differential equations (PDEs). The finite-difference method is a numerical technique used to approximate solutions to these PDEs. We consider a simple linear form of Turing pattern PDEs for two interacting chemical species with concentrations $u(x, y, t)$ and $v(x, y, t)$:

$$\begin{aligned} \frac{\partial u}{\partial t} &= f(u, v) + D_u \nabla^2 u, \\ \frac{\partial v}{\partial t} &= g(u, v) + D_v \nabla^2 v, \end{aligned}$$

where $f(u, v)$ and $g(u, v)$ are the reaction terms, and D_u and D_v are the diffusion coefficients.

We discretize the spatial domain into a grid with points (x_i, y_j), where $x_i = i\Delta x$, $y_j = j\Delta y$, and i, j are integers. The Laplacian ∇^2 in two dimensions is discretized using the central difference scheme:

$$\nabla^2 u \approx \frac{u_{i+1,j} + u_{i-1,j} + u_{i,j+1} + u_{i,j-1} - 4u_{i,j}}{\Delta x^2},$$

assuming $\Delta x = \Delta y$ for simplicity.

We discretize time into steps of size Δt. The time derivative is approximated using the forward difference:

$$\frac{\partial u}{\partial t} \approx \frac{u_{i,j}^{n+1} - u_{i,j}^{n}}{\Delta t},$$

where superscripts denote time levels.

Substituting the discretized derivatives into the PDEs, we obtain the finite-difference equations:

$$\begin{aligned}
\frac{u_{i,j}^{n+1} - u_{i,j}^{n}}{\Delta t} &= f(u_{i,j}^{n}, v_{i,j}^{n}) + D_u \frac{u_{i+1,j}^{n} + u_{i-1,j}^{n} + u_{i,j+1}^{n} + u_{i,j-1}^{n} - 4u_{i,j}^{n}}{\Delta x^2}, \\
\frac{v_{i,j}^{n+1} - v_{i,j}^{n}}{\Delta t} &= g(u_{i,j}^{n}, v_{i,j}^{n}) + D_v \frac{v_{i+1,j}^{n} + v_{i-1,j}^{n} + v_{i,j+1}^{n} + v_{i,j-1}^{n} - 4v_{i,j}^{n}}{\Delta x^2}.
\end{aligned}$$

Rearranging these equations gives the update formulas for u and v at each time step.

The stability of the explicit finite-difference scheme is crucial. For nonlinear systems like Turing patterns the time step Δt must be chosen carefully relative to the spatial discretization Δx to ensure stability. The diffusion terms typically impose a restriction of the form $\Delta t \propto \Delta x^2/D$, where D is the diffusion coefficient.

The truncation error in the finite-difference approximation is of order $O(\Delta x^2)$ for the spatial derivatives and $O(\Delta t)$ for the time derivative.

References

Alan M Turing. The chemical basis of morphogenesis. *Philosophical Transactions of the Royal Society of London. Series B, Biological Sciences*, 237(641):37–72, 1952.

Alfred Gierer and Hans Meinhardt. A theory of biological pattern formation. *Kybernetik*, 12:30–39, 1972.

Michael F. Staddon. How the zebra got its stripes: Curvature-dependent diffusion orients turing patterns on three-dimensional surfaces. *Physical Review E*, 110(3):034402, 2024. doi: 10.1103/PhysRevE.110.034402.

Shigeru Kondo, Masakatsu Watanabe, and Seita Miyazawa. Studies of turing pattern formation in zebrafish skin. *Philosophical Transactions of the Royal Society A: Mathematical, Physical and Engineering Sciences*, 379(2216):20200274, 2021. doi: 10.1098/rsta.2020.0274. URL `https://doi.org/10.1098/rsta.2020.0274`.

Akiko Nakamasu, Go Takahashi, Akio Kanbe, and Shigeru Kondo. Interactions between zebrafish pigment cells responsible for the generation of turing patterns. *Proceedings of the National Academy of Sciences*, 106(21):8429–8434, 2009. doi: 10.1073/pnas.0808622106.

Ebrahim Jahanbakhsh and Michel C. Milinkovitch. Modeling convergent scale-by-scale skin color patterning in multiple species of lizards. *Current Biology*, 32(23):R1306–R1308, 2022. doi: 10.1016/j.cub.2022.10.044.

P.K. Maini and T.E. Woolley. The turing model for biological pattern formation. In A. Bianchi, T. Hillen, M. Lewis, and Y. Yi, editors, *The Dynamics of Biological Systems*, volume 4 of *Mathematics of Planet Earth*. Springer, Cham, 2019. doi: 10.1007/978-3-030-22583-4_7. URL `https://doi.org/10.1007/978-3-030-22583-4_7`.

Benjamin M. Alessio and Ankur Gupta. Diffusiophoresis-enhanced turing patterns. *Science Advances*, 9(45):adj2457, Nov 2023. doi: 10.1126/sciadv.adj2457. URL `https://doi.org/10.1126/sciadv.adj2457`.

Y. Benenson. Challenges in integrating turing-like patterns in biomolecular computing systems: Complexity in representing biological processes and molecular machines. *Nature Reviews Genetics*, 2012. URL `https://www.nature.com/articles/nrg3197`.

M. Tanaka, S.M. Montgomery, L. Yue, et al. Framework for applying turing patterns in synthetic biology: Streamlined data integration to retain fidelity across biological scales. *Science Advances*, 2023. URL `https://www.science.org/doi/abs/10.1126/sciadv.ade4381`.

A. Volkening. Survey on self-organization quantification and the integration of turing patterns in stochastic biological systems. *arXiv*, 2024. URL `https://arxiv.org/pdf/2407.10832`.

A. Diez, A.L. Krause, P.K. Maini, E.A. Gaffney, and S. Seirin-Lee. Exploring turing pattern formation in reaction-cross-diffusion models: Stability effects of growth terms and scaling mechanisms for pattern coherence. *bioRxiv*, 2023. URL `https://www.biorxiv.org/content/10.1101/2023.05.30.542795.pdf`.

S. Werner, T. Stückemann, M. Beirán Amigo, and J.C. Rink. Scaling and regeneration of self-organized turing patterns under feedback mechanisms and environmental perturbations. *arXiv*, 2015. URL `https://arxiv.org/pdf/1411.2359`.

S. Kondo. Updated turing model for biological pattern formation: Addressing limitations in reaction-diffusion models for specific biological environments. *Journal of Theoretical Biology*, 2017. URL `https://www.sciencedirect.com/science/article/pii/S0022519316303630`.

A.L. Krause and E.A. Gaffney. Advances in turing's morphogenesis theory: Adapting models to complex biological dynamics. *Philosophical Transactions of the Royal Society A*, 2021. URL `https://royalsocietypublishing.org/doi/abs/10.1098/rsta.2020.0280`.

M. Rietkerk et al. Spatial pattern formation in ecological systems: Challenges of turing model adaptation to large-scale dynamics. *Science*, 2021. URL `https://research.rug.nl/files/193917119/science.abj0359.pdf`.

Michel C Milinkovitch, Ebrahim Jahanbakhsh, and Szabolcs Zakany. The unreasonable effectiveness of reaction diffusion in vertebrate skin color patterning. *Annual Review of Cell and Developmental Biology*, 39:145–174, 2023. doi: 10.1146/annurev-cellbio-120319-024414. URL https://doi.org/10.1146/annurev-cellbio-120319-024414.

Philip K Maini. Using mathematical models to help understand biological pattern formation. *Comptes rendus. Biologies*, 327(3):225–234, 2004.

Václav Klika. Significance of non-normality-induced patterns: Transient growth versus asymptotic stability. *Chaos: An Interdisciplinary Journal of Nonlinear Science*, 27(7): 073120, 2017. doi: 10.1063/1.4985256. URL https://doi.org/10.1063/1.4985256.

EA; Jewell-TJ; Klika V; Walker BJ Krause, AL; Gaffney. Turing instabilities are not enough to ensure pattern formation. *Bulletin of Mathematical Biology*, 86(21), 2024. doi: 10.1007/s11538-023-01250-4.

Yanyan Chen and Javier Buceta. A non-linear analysis of turing pattern formation. *PLoS ONE*, 14(8):e0220994, 08 2019. doi: 10.1371/journal.pone.0220994. URL https://doi.org/10.1371/journal.pone.0220994.

J. L. Aragón, R. A. Barrio, T. E. Woolley, R. E. Baker, and P. K. Maini. Nonlinear effects on turing patterns: Time oscillations and chaos. *Phys. Rev. E*, 86(2):026201, 2012. doi: 10.1103/PhysRevE.86.026201. URL https://doi.org/10.1103/PhysRevE.86.026201.

Martina Oliver Huidobro and Robert G. Endres. Effects of multistability, absorbing boundaries and growth on turing pattern formation. *bioRxiv*, 2024. doi: 10.1101/2024.09.09.611947. URL https://doi.org/10.1101/2024.09.09.611947.

Roozbeh H. Pazuki and Robert G. Endres. Robustness of turing models and gene regulatory networks with a sweet spot. *Phys. Rev. E*, 109:064305, 2024. doi: 10.1103/PhysRevE.109.064305. URL https://doi.org/10.1103/PhysRevE.109.064305.

Shibashis Paul, Joy Adetunji, and Tian Hong. Widespread biochemical reaction networks enable turing patterns without imposed feedback. *Nature Communications*, 14, 2023.

Jasper van der Kolk, Guillermo García-Pérez, Nikos E. Kouvaris, M. Ángeles Serrano, and Marián Boguñá. Emergence of geometric turing patterns in complex networks. *Physical Review X*, 13(021038), 2023. doi: 10.1103/PhysRevX.13.021038.

Ajay Subbaroyan, Olivier C. Martin, and Areejit Samal. Minimum complexity drives regulatory logic in boolean models of living systems. *PNAS Nexus*, 1(1):pgac017, 2022. doi: 10.1093/pnasnexus/pgac017.

Pascal F. Hagolani, Roland Zimm, Renske Vroomans, and Isaac Salazar-Ciudad. On the evolution and development of morphological complexity: A view from gene regulatory networks. *Journal of Theoretical Biology*, 2023.

Saverio Forestiero. The historical nature of biological complexity and the ineffectiveness of the mathematical approach to it. *Acta Biotheoretica*, 2022. doi: 10.1007/s12064-022-00369-7.

S. Miyazawa, M. Okamoto, and S. Kondo. Blending of animal colour patterns by hybridization. *Nature Communications*, 1(66):1–7, 2010. doi: 10.1038/ncomms1071.

D.E. Lee, D.R. Cavener, and M.L. Bond. Seeing spots: quantifying mother-offspring similarity and assessing fitness consequences of coat pattern traits in a wild population of giraffes. *PeerJ*, 6:e5690, 2018. doi: 10.7717/peerj.5690.

T. Glimm, M. Kiskowski, N. Moreno, and Y. Chiari. Capturing and analyzing pattern diversity: an example using the melanistic spotted patterns of leopard geckos. *PeerJ*, 9: e11829, 2021. doi: 10.7717/peerj.11829.

G.H. Moro, M. de Gomensoro Malheiros, and M. Walter. Quantitative descriptors for a range of visual biologic pigmentation patterns. In *35th SIBGRAPI Conference on Graphics, Patterns and Images*, pages 133–138, 2022. doi: 10.1109/SIBGRAPI55357.2022.9991769.

B. Ermentrout. Stripes or spots? nonlinear effects in bifurcation of reaction–diffusion equations on the square. *Proceedings of the Royal Society A*, 434(1891):413–417, 1991.

T.J. Callahan and E. Knoblauch. Pattern formation in reaction–diffusion systems: a bifurcation analysis. *Journal of Mathematical Biology*, 48(4):385–417, 2004. doi: 10.1007/s00285-003-0240-8.

P. Gray and S. K. Scott. Autocatalytic reactions in the isothermal, continuous stirred tank reactor: isolas and other forms of multistability. *Chemical Engineering Science*, 38(1): 29–43, 1983. doi: 10.1016/0009-2509(83)80194-7.

John E. Pearson. Complex patterns in a simple system. *Science*, 261(5118):189–192, 1993. doi: 10.1126/science.261.5118.189.

Robert E. Munafo. Generalized Gray–Scott models. *Complex Systems*, 27(4):315–367, 2018. doi: 10.25088/ComplexSystems.27.4.315.

John J. Mueller and Eshel Ben-Jacob. Dissipative structures and morphogenesis in bacterial colonies. *Physica A*, 249(1–4):123–130, 1998. doi: 10.1016/S0378-4371(97)00568-3.

J. S. McGough and K. Riley. Pattern formation in the gray–scott model. *Nonlinear Analysis: Real World Applications*, 5(1):105–121, 2004. doi: 10.1016/S1468-1218(03)00020-8.

S. Li M. Zheng and B. Xu. High-fidelity simulations for turing pattern formation in multidimensional gray-scott reaction-diffusion system. *Computers & Mathematics with Applications*, 80(7):1611–1621, 2020. doi: 10.1016/j.camwa.2020.07.020.

Q. Yang J. Li and Y. Zhang. Uniform patterns formation based on gray-scott model for 3d printing. *Journal of Applied Mathematics and Physics*, 7(12):2884–2895, 2019. doi: 10.4236/jamp.2019.712198.

Alan Hodgkin and Andrew Huxley. A quantitative description of membrane current and its application to conduction and excitation in nerve. *J. Physiol.*, 117(4):500–544, 1952.

Richard FitzHugh. Impulses and physiological states in theoretical models of nerve membrane. *Biophys. J.*, 1(6):445–466, 1961.

Suguru Arimoto Jinichi Nagumo and Shuji Yoshizawa. An active pulse transmission line simulating nerve axon. *Proc. IRE*, 50(10):2061–2070, 1962.

Daniel Ruiz-Reynes Daniel Cebrian-Lacasa, Pedro Parra-Rivas and Lendert Gelens. Six decades of the fitzhugh-nagumo model: A guide through its spatio-temporal dynamics and influence across disciplines. *arXiv preprint arXiv:2404.11403*, 2024. URL `https://arxiv.org/abs/2404.11403`.

Gaetana Gambino, Maria Cristina Lombardo, Gino Rubino, and Marcello Sammartino. Pattern selection in the 2d fitzhugh–nagumo model. *Ricerche di Matematica*, 67(2):377–392, 2018. doi: 10.1007/s11587-018-0424-6.

Ben D MacArthur, Avi Ma'ayan, and Ihor R Lemischka. Systems biology perspectives on stem cell fate. *Nature Reviews Molecular Cell Biology*, 10(9):672–681, 2009.

Johan Paulsson. Summing up the noise in gene networks. *Nature*, 427(6973):415–418, 2004.

Imke Roeder and Ingmar Glauche. Modeling stem cell behavior with bayesian inference. *Nature*, 441:435, 2006.

J Lynn Cherry and Frederick R Adler. How to make a biological switch. *Journal of Theoretical Biology*, 203(2):117–133, 2000.

Understanding gene circuits at cell-fate branch points for rational cell reprogramming. *Trends in Genetics*, 27(2):55–62, 2011. ISSN 0168-9525. doi: https://doi.org/10.1016/j.tig.2010.11.002.

Ruben Perez-Carrasco, Pilar Guerrero, James Briscoe, and Karen Page. Intrinsic noise profoundly alters the dynamics and steady state of morphogen-controlled bistable genetic switches. *PLoS Computational Biology*, 12(8):e1005154, 2016.

Patrick B Warren and Pieter Rein ten Wolde. Statistical analysis of the spatial patterns of cell-to-cell communication. *Journal of Computational Biology*, 11(2-3):308–325, 2004.

Thomas B Kepler and Timothy C Elston. Stochasticity in transcriptional regulation: origins, consequences, and mathematical representations. *Biophysical Journal*, 81(6):3116–3136, 2001.

Vijay Chickarmane, Tariq Enver, and Carsten Peterson. A bistable switch in myeloid differentiation. *Journal of Theoretical Biology*, 244(1):68–76, 2006.

Michael K Strasser, Fabian J Theis, and Carsten Marr. Stability and multi-attractor dynamics of a toggle switch based on a two-stage model of stochastic gene expression. *Biophysical Journal*, 101(3):611–621, 2011.

Ming-Chang Huang, Jinn-Wen Wu, Yu-Pin Luo, and Karen G Petrosyan. Fluctuations in gene regulatory networks as gaussian colored noise. *Journal of Chemical Physics*, 130(14): 145101, 2009.

Ushasi Roy, Divyoj Singh, Navin Vincent, Chinmay K Haritas, and Mohit Kumar Jolly. Spatiotemporal patterning enabled by gene regulatory networks. *ACS Omega*, 8(4):3713–3725, 2023. doi: 10.1021/acsomega.2c04581. URL `https://doi.org/10.1021/acsomega.2c04581`.

Makoto Sato, Tetsuo Yasugi, Yoshiaki Minami, and Masaharu Nagayama. Notch-mediated lateral inhibition regulates proneural wave propagation when combined with egf-mediated reaction diffusion. *Proceedings of the National Academy of Sciences*, 113(35):E5153–E5162, August 2016. doi: 10.1073/pnas.1602739113. URL `https://doi.org/10.1073/pnas.1602739113`.

Ming Li and Paul Vitányi. *An Introduction to Kolmogorov Complexity and Its Applications*. Springer, 3rd edition, 2008.

Paul M. B. Vitányi. Kolmogorov complexity. In Vasco Brattka, Peter Hertling, and Klaus Weihrauch, editors, *Handbook of Computability and Complexity in Analysis*, pages 381–454. Springer, 2021. doi: 10.1007/978-3-030-59234-9_10.